

## Chapter 2

# Thin dielectric films stress extraction

Residual stress in thin films is a major concern for the operation and the reliability of MEMS. Various methods have been published these last years to extract the residual stress in polysilicon [27][54][55][56][57]. Nowadays, other types of materials such as  $\text{SiO}_2$  or  $\text{Si}_x\text{N}_y$  are also being used in MEMS as structural material, especially in the fabrication of suspended membranes for pressure or microheaters based sensors. Residual stress can be compressive, which makes the film expand parallel to the surface, or tensile, which makes the film shrink. The profile as well as the robustness of a thin dielectric membrane are affected by the residual stress. A too compressive membrane may buckle, avoiding its use to support sensors. A too tensile membrane can break in presence of pressure or high temperature gradients. It is therefore essential to be able to measure and control the stress separately in each layer composing the structure in order to design reliable multilayers.

The use of stress values extracted from the literature is not sufficient since materials properties can change a lot from one piece of equipment to another as well as between two processes. It is therefore not only necessary to characterize the silicon oxide and the silicon nitride produced in each laboratory but also essential to be able to measure the stress during each fabrication batch on processed wafers.

This chapter reports our detailed study on the residual stress in the thin dielectric films constituting a typical released membrane: thermal oxide, LPCVD nitride and PECVD oxide<sup>1</sup>. Residual stresses in oxide have not been much studied so far since oxide is mainly used as a sacrificial layer for the release of structures in polysilicon, nitride or metal or as a non dominant part of a thick silicon membrane. Stress measurements in nitride films, on

---

<sup>1</sup>Oxide and nitride will be used from now on as abbreviated forms of respectively silicon oxide and silicon nitride.

the other hand, are more common and a lot of methodologies are available. Nevertheless, measurements of these dielectric films at very low thicknesses as in their actual use are not so common. And stress measurements for the combinations of these layers are even more rare.

Two measurement methods are presented and compared in this chapter. The first one is the well known substrate curvature technique [27], generalized to extract the residual stress in thin stacked films. This technique also demonstrates how to extract the residual stress in the buried oxide of a SOI wafer and in the membrane at the end of our complete gas sensor process. The second one is based on micromachined microstructures [54] designed for our purpose, i.e. characterization of the stress in very thin dielectric layers. The anisotropic silicon etching properties of the CMOS compatible etchant TMAH were used to release strain measurement structures made in thin films of oxide, nitride, as well as a combination of each of them on silicon. The variation of stress throughout the membrane thickness was finally investigated with dedicated microstructures.

But in order to support the correct interpretations of our experimental results, we think interesting to firstly summarize the main theoretical concepts of thin films mechanics useful for MEMS researchers and designers.

## 2.1 Introduction - Definitions

### 2.1.1 Stress, strain and Elastic constants

**Stress**  $\sigma$  is the force per unit area that is acting on a surface of a solid, more commonly expressed in Pascals ( $Pa$ ) or  $N/m^2$ .

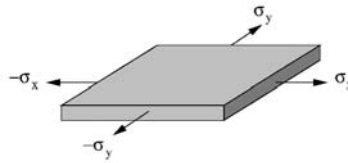


Figure 2.1: Stress on a differential volume in static equilibrium.

In case of a thin film on a thick substrate, no stress will occur in the direction  $z$ , normal to the substrate, as a film under stress can only expand or contract by bending

the substrate and deforming it in a vertical direction [27]. The plate is thin enough to avoid any variation of displacement with respect to  $z$ . Vertical deformations will not induce stresses in a substrate because it freely moves in that direction. We call this state plane stress. In such a biaxial system  $(x, y)$ , the shear stress (acting along the surface) can also be eliminated [58]. We finally assume that no significant external forces act on the system. This means that the surface forces on opposite sides of the structure must be equal as shown in Fig. 2.1. In other words, the system is in static equilibrium. The two elements of stress can be therefore represented as the following matrix

$$\sigma = \begin{pmatrix} \sigma_x & 0 \\ 0 & \sigma_y \end{pmatrix} \quad (2.1)$$

Stresses can be the result of externally applied forces. In this case, after the load is removed, the stresses are expected to vanish. On the other hand, thin films are stressed even without the application of externally imposed forces and are characterized by an internal or **residual stress** [59] as we will explain further. In the following sections, all stresses will be supposed to be residual stresses. Residual stress can be compressive or tensile. By convention, stress in first case will be expressed with a minus sign and in second case, with a positive sign.

When subjected to a stress, any free body literally get pushed (or pulled) out of shape. **Strain**  $\varepsilon$  is a measure of this deformation [11]. It is therefore defined in terms of the partial derivatives of the displacement. Strain is a dimensionless variable. In static equilibrium, the strain is caused by stress, so the principal coordinate system is the same for stress and strain [58].

Materials of interest (silicon, oxide and nitride) being completely elastic (and no plastic), they obey to Hook's law; that means, they deform linearly with load. Since load is proportional to stress and deformation is proportional to strain, stress and strain are linearly related:

$$\begin{pmatrix} \varepsilon_x \\ \varepsilon_y \end{pmatrix} = \begin{pmatrix} H_{11} & H_{12} \\ H_{21} & H_{22} \end{pmatrix} \begin{pmatrix} \sigma_x \\ \sigma_y \end{pmatrix} = H \begin{pmatrix} \sigma_x \\ \sigma_y \end{pmatrix} \quad (2.2)$$

From our previous assumptions,  $H$  matrix has only two independent elements or two

elastic constants: the elastic modulus or Young's Modulus  $E$  and the Poisson ratio  $\nu$ .

$$H = \begin{pmatrix} 1/E & -\nu/E \\ -\nu/E & 1/E \end{pmatrix} \quad (2.3)$$

Eq.2.2 can therefore be reduced to the following strain-stress relationships :

$$\begin{aligned} \varepsilon_x &= \frac{1}{E} (\sigma_x - \nu \sigma_y) \\ \varepsilon_y &= \frac{1}{E} (\sigma_y - \nu \sigma_x) \end{aligned} \quad (2.4)$$

In an isotropic material<sup>2</sup>,  $\varepsilon = \varepsilon_x = \varepsilon_y$  so that the in-plane or **biaxial stress**  $\sigma = \sigma_x = \sigma_y$  is equal to

$$\sigma = \left( \frac{E}{1 - \nu} \right) \varepsilon \quad (2.5)$$

The ratio  $E/1 - \nu$  is called the **biaxial modulus**.

This equation is valid for the specific boundary conditions seen by a thin film on a rigid substrate. If the film was subjected only to **uniaxial stress** (i.e. the film is restricted to move only in one direction), the stress is simply

$$\sigma = E \varepsilon \quad (2.6)$$

However, this equation can rarely be used in presence of internal residual stress since stress in this case is a thermal or growing effect in all directions instead of a traction or contraction due to an external load.

The **elastic modulus** or **Young's Modulus**  $E$  tells us how much a material is elongated under a given load. It has units of force per unit of area, just like stress and pressure. It may also be thought as the stiffness or material resistance to elastic deformation. The higher the material elastic modulus, the lesser it deforms for a given stress, and thus the stiffer it is. For example, an incompressible material would have an infinite Young's modulus, while a "soft" material would deform considerably for a given amount of stress, so its modulus of elasticity would be quite low [11].

Under uniaxial tensile stress, the element expands in the direction of the stress, and contracts in directions perpendicular to the stress. In this situation, there are two strains,

---

<sup>2</sup>Or in a cubic crystal like silicon in case of our previous assumptions.

one axial and one transverse. The ratio of the transverse to the axial strains, or the proportionality between the contraction and the elongation, is the **Poisson ratio**  $\nu$ . This ratio is dimensionless, and has a value between 0.2 and 0.5 for most materials. The volume of the element has changed as a consequence of the strain. The volume expansion is proportional to  $(1 - 2\nu)$ , which means that materials with  $\nu = 0.5$  does not change their volume under uniaxial stress and are called incompressible [58][11].

Table 2.1 gives the elastic constants generally accepted for some common MEMS materials. The Young's modulus and Poisson ratio of silicon are dependent on its crystallographic orientation and can vary according to the direction in a given plane (such as in  $\{100\}$  planes). However, biaxial modulus is constant in the (100) plane as demonstrated in details in [60] and is equal to **180.5 GPa**. The silicon Young's modulus and Poisson ration in the  $\langle 100 \rangle$  crystallographic directions (as cited in Table 2.1) are commonly measured by various methods and calculated in [61][33] or mentionned in [13][62]. These values are more consistent than a lot of others cited without reference to any crystallographic plane (as in [58][27][11]). Furthermore, the silicon Young's modulus values calculated by nanoindentation (as in [63]) are not convincing since they depend on the silicon doping level and the applied load. That was also confirmed by measurements performed in our lab. As explained in [64], the silicon phase changes during indentation and results in a modification of the Young's modulus value.

Table 2.1: Mechanical properties of some important MEMS materials.

Material	Young's modulus [GPa]	Poisson ratio [s.d.]	Source
<b>Silicon (100)</b>	130	0.28	[60][61][33][13][62]
<b>Polysilicon</b>	160	0.23	[65][27][59][58][11]
<b>Silicon dioxide</b>	70	0.20	[65][27][59][58][11]
<b>Stoichiometric LPCVD nitride</b>	270	0.27	[65][27][59][58][11]
<b>Aluminum</b>	70	0.35	[65][27][59][58][11]

Elastic constants of the other materials mentioned in Table 2.1 are less object of discussion. Nevertheless, the commonly available tabulated values of mechanical properties of materials are generally derived from bulk specimens, and thus may not be very relevant to the materials and scales used in micromachined devices [11]. But good approximations can be made with these available data.

Existing methods to extract elastic modulus and Poisson ratio in thin films made of harder materials are the bending beam and resonant beam methods [62][1]. The first one consists in loading the tip of a cantilever beam using a nanoindenter (as is called a load controlled submicrometer indentation instrument [1]) and to measure the force-displacement curve to finally extract the Young's modulus [62]. In the second method, the Young's modulus is obtained by measuring the resonant frequency of a beam under excitation [62]. Both methods can also advantageously be used to extract the Young's modulus for each layer of multi-layered cantilevers without accessing the individual layers during processing as demonstrated in [66] and [65]. The Poisson ratio for thin films is more difficult to measure than the Young's modulus as thin films tend to bend out of plane in response to in-plane shear [27]. Fortunately, it is not required to know Poisson ratio in order to extract stress in most microstructures as we will see further.

As process parameters greatly influence these elastic properties and may be difficult to reproduce on one set of equipment, let alone on the equipment of others [11], they might be usefully measured in the thin films under consideration. Nevertheless, the Young's moduli of the layers under consideration in our work are generally well known and will be used here.

### 2.1.2 Uniform and non-uniform stresses and strains in thin films

Residual stress can be uniform or non-uniform through the depth of a thin film. If the stress is uniform, its measurement will give an **average stress**. If the stress is non uniform, a difference of stress or **stress gradient** exists between the top and the bottom of the thin film. Using dedicated methods, this stress gradient can be isolated and measured, otherwise, the measured stress will be an average stress through the depth taking into account the vertical variation of stress.

Uniform stress will produce a deformation and therefore a proportional **average relaxed strain**. In the same way, a stress gradient will lead to a **relaxed strain gradient**. If a body is stressed but not free to move, it will not be allowed to relax, and no deformation and therefore no relaxed strain will be able to occur. The body is said under residual stress and therefore under residual strain proportional to the residual stress, but without relaxed strain. If the same stressed body is now allowed to move, it will lead to relax until an equilibrium state, and a deformation will occur. In this case, the stress is vanished and was replaced by a relaxed strain. So, it is important to note our distinction between the **strain** equal to the stress on Young's modulus ratio and present in same time that the

stress, and the **relaxed strain** equal to the strain in absolute value but compensating the strain and therefore of opposite sign. Both strains are mathematically identical but the use of two different terms will facilitate its understanding. We will see along this chapter one technique to measure stress by transformation of stress into relaxed strain through the release of a microstructure.

Nearly all films have a state of residual stress, due to mismatch in the thermal expansion coefficient between the film and the substrate, to lattice mismatch, to substitutional or interstitial impurities, to growth processes, etc. [27]. All factors of stresses can be classified in two groups: **extrinsic** and **intrinsic** stresses.

### Extrinsic stress

The extrinsic stress is imposed by unintended external factors such as temperature gradients. It is commonly uniform through the depth. **Thermal-mismatch stress** is the more common source of extrinsic stress and is well understood. It specially arises in structures with inhomogeneous thermal expansion coefficients, subjected to uniform temperature change.

To understand the causes and effects of thermal-mismatch stress in thin films, consider the typical structure shown in Fig. 2.2.

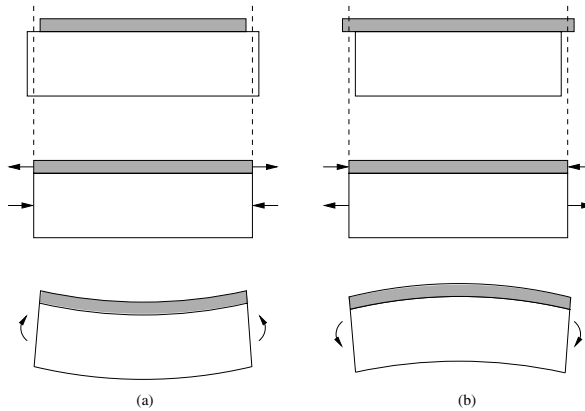


Figure 2.2: Sequence of events leading to (a) residual tensile stress in film; (b) residual compressive stress in film (adapted from [59]).

Considering, as it is often the case, that the thin film was deposited on the substrate

at an elevated temperature. In general the thin film and substrate have different **thermal expansion coefficients**. The thermal expansion coefficient of a material is defined as

$$\alpha = \frac{d\varepsilon}{dT} \quad (2.7)$$

Assuming that the thermal expansion coefficients are temperature independent, the strain caused by thermal expansion is then simplify

$$\varepsilon(T) = \varepsilon(T_0) + \alpha \cdot \Delta T \quad (2.8)$$

where the first part of the equation is assumed to be negligible and the last part, the strain caused by thermal expansion.

When a thin film is deposited on a thick substrate at elevated temperature, and subsequently cooled and operated at ambient temperature, the difference between the thermal expansion coefficients of the film and substrate creates stress and strain.

First consider the behavior shown in Fig. 2.2(a) where the growing film initially shrinks relative to the substrate. Usually, the substrate dimensions undergo minor shrinkage in the plane while the film dimensions may reduce significantly. Compatibility, however, requires that both the film and substrate have the same length. Therefore, the film is constrained and stretches, while the substrate accordingly contracts. The tensile forces developed in the film are balanced by the compressive forces in the substrate. However, the combination is still not in mechanical equilibrium because of the uncompensated end moments. To remind you, equilibrium requires that forces ( $F$ ) and bending moments ( $M$ ) vanish on any film/substrate cross section. If the structure is free to move, it will elastically bend to counteract the unbalanced moments. Thus, films containing internal **tensile stresses** bend the substrate concave upward. Similarly, **compressive stresses** lead their origin from films that tend to initially expand relative to the substrate (Fig. 2.2(b)). Internal compressive stresses, therefore, bend the substrate convex outward [59].

As the substrate is very thick compared to the film, it is a good approximation to assume that the substrate contracts to the size it would have attained in absence of the film [58]. With this assumption, we can write the strain of the substrate as

$$\varepsilon_s = -\alpha_s \cdot \Delta T \quad (2.9)$$

where  $\alpha_s$  represents the coefficient of thermal expansion for the substrate and the minus



sign, the compression of the film. The film then gets this same strain due to the fact that it is attached to the substrate.

$$\varepsilon_{f,attached} = -\alpha_s \cdot \Delta T \quad (2.10)$$

If the film was unattached, however, its strain would be

$$\varepsilon_{f,free} = -\alpha_f \cdot \Delta T \quad (2.11)$$

where  $\alpha_f$  represents the coefficient of thermal expansion for the thin film.

The difference between the strains film features with and without attachment to the substrate is the thermal mismatch strain [58]

$$\varepsilon_{f,mismatch} = \varepsilon_{f,attached} - \varepsilon_{f,free} = (\alpha_f - \alpha_s) \cdot \Delta T \quad (2.12)$$

The thermal mismatch leads to stress in the film. From previous equation, we can write in case of biaxial system

$$\sigma_{f,mismatch} = \frac{E}{1 - \nu} (\alpha_f - \alpha_s) \cdot \Delta T \quad (2.13)$$

By convention, tensile stress is positive, compressive stress is negative. Therefore, if  $\alpha_f < \alpha_s$ , a compressive stress will be expected and if  $\alpha_f > \alpha_s$ , a tensile stress will appear.

### **Intrinsic stress**

The intrinsic stress reflects the internal structure of a material during its deposition. It is less clearly understood than the thermal stress. It depends on deposition rate, deposition temperature, pressure in the deposition chamber, incorporation of impurities during growth, grain structure, fabrication process defects, etc. In most cases, intrinsic stress is non uniform through the depth and is therefore responsible of stress gradient.

For instance, the phosphorous doped polysilicon is expected to be more compressive than pure polysilicon because the phosphorous atom is larger than silicon [27]. Boron is another dopant in silicon which exerts a tensile stress when introduced into the crystal lattice. As the smaller boron atom displaces the silicon atom, there is a tendency for the lattice to contract locally. However the silicon lattice will restrain from contracting and therefore results in a local tensile stress. High level of boron concentration is usually used as etch stop for controlling the depth in silicon substrate of the height of a silicon

beam which generates high levels of stress gradient since the vertical dopant profile is not uniform and causes therefore a stress distribution varying with depth [67]. During layers deposition, microvoids can also appear when by-products escape as gases and the lateral diffusion of atoms evolves too slowly to fill all the gaps, resulting in a tensile film [27]. Finally, thermal oxide shows stress gradient due to oxygen diffusion while the film is forming [68] but is in same time under compressive stress due to the fact that in the oxide layer one silicon atom takes nearly twice as much space as in single crystalline silicon [27].

Intrinsic stress can sometimes be annealed out completely but the anneal temperatures are quite high and may not be practical for the production of micromechanical devices [13]. On the contrary, some amount of thermal mismatch stress is unavoidable when working with materials having different thermal expansion coefficients.

## 2.2 Stress measurements by substrate curvature method

### 2.2.1 Theory

We consider a composite plate film/substrate of width  $w$  [59][69] as in Fig. 2.3.

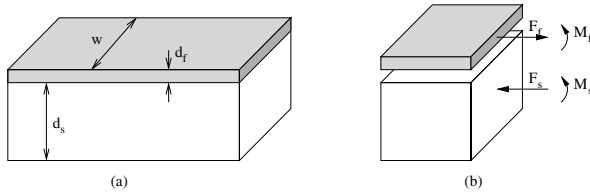


Figure 2.3: Stress analysis of film/substrate combination: (a) structure; (b) free-body diagrams of film and substrate with forces and end moments (adapted from [59]).

The film thickness and Young's modulus are  $d_f$  and  $E_f$ , respectively, while the corresponding substrate values are  $d_s$  and  $E_s$ . Due to internal stresses, mismatch forces arise at the film/substrate interface. As seen on Fig. 2.3, each set of forces can be replaced by the static equivalent combination of a force and moment;  $F_f$  and  $M_f$  in the film,  $F_s$  and  $M_s$  in the substrate, where  $F_f = F_s$  since film and substrate are stucked together. Force  $F_f$  can be considered to act uniformly over the cross-sectional area  $d_f.w$ , or on the middle

of this section at  $\frac{d_f}{2}$ . In this case, equilibrium requires that

$$F_f \cdot \frac{d_f}{2} = M_f \quad (2.14)$$

or for the complete structure

$$F_f \cdot \frac{(d_f + d_s)}{2} = M_f + M_s \quad (2.15)$$

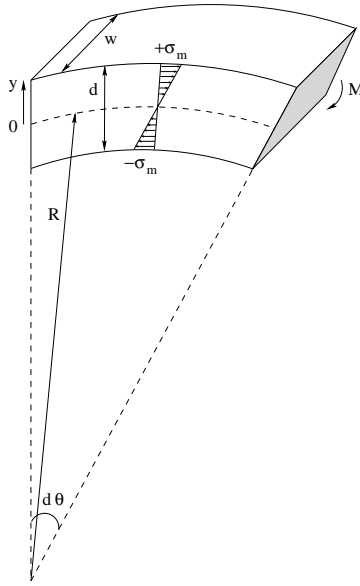


Figure 2.4: Elastic bending of a beam under applied moment (adapted from [59]).

Considering now an isolated beam segment bent by a moment  $M$  (Fig. 2.4), the deformation is assumed to entirely consist of the extension or contraction of longitudinal beam fibers by an amount proportional to their distance from the central or neutral axis, which remains unstrained in the process. The stress distribution reflects this by varying linearly across the section from maximum tension  $+\sigma_m$  on the top to maximum compression  $-\sigma_m$  on the bottom [59].

The length of the neutral axis where the stress equals zero, is given by

$$L_{y=0} = R.d\theta \quad (2.16)$$

where  $R$  is the radius of curvature of the beam segment and  $d\theta$ , the subtended angle. The length of the section at an arbitrary position  $y$  is

$$L_y = (R + y) .d\theta \quad (2.17)$$

The strain along the  $y$  axis is the difference between the length of the neutral axis and the length at position  $y$

$$\varepsilon_y = \frac{L_y - L_{y=0}}{L_{y=0}} = \frac{(R + y) .d\theta - R.d\theta}{R.d\theta} = \frac{y}{R} \quad (2.18)$$

The axial stress is then given by combination of 2.6 and 2.18

$$\sigma_y = E \frac{y}{R} \quad (2.19)$$

and the maximum stresses on the top and bottom of the beam are therefore equal to

$$\sigma_m = \pm E \frac{d}{2R} \quad (2.20)$$

showing that compressive stress on the top is negative and tensile stress on the bottom is positive.

We can now calculate the bending moment of the beam segment by integrating the stress over the beam section.

$$M = 2 \int_0^{d/2} \sigma_y w.y dy = E \frac{d^3 w}{12R} = \frac{E}{R} I \quad (2.21)$$

where  $I = \frac{wd^3}{12}$  is called the **moment of inertia** of a rectangular beam with respect to the center of the beam in a direction perpendicular to one of the sides [69]. By extension of this result, we have

$$M_f = E_f \frac{d_f^3 w}{12R} \quad \text{and} \quad M_s = E_s \frac{d_s^3 w}{12R} \quad (2.22)$$

Finally, in order to account for actual biaxial-stress distribution in films, rather than the uniaxial stresses assumed for ease of integration, it is necessary to replace  $E_f$  by  $E_f/(1 - \nu_f)$

and similarly for  $E_s$ . Substitution of these terms in Eq. 2.15 yields

$$F_f \cdot \frac{(d_f + d_s)}{2} = E_f \frac{d_f^3 w}{12R(1 - \nu_f)} + E_s \frac{d_s^3 w}{12R(1 - \nu_s)} \quad (2.23)$$

Since  $d_s$  is normally much larger than  $d_f$ , the equation becomes

$$F_f \cdot \frac{d_s}{2} = E_s \frac{d_s^3 w}{12R(1 - \nu_s)} \quad (2.24)$$

Furthermore, since  $\sigma_f$  is equal to the force  $F_f$  acting on the area  $wd_f$  or  $\sigma_f = F_f/wd_f$ , the film stress  $\sigma_f$  can be then given by

$$\sigma_f = \frac{E_s d_s^2}{6(1 - \nu_s)} \cdot \frac{1}{d_f} \cdot \frac{1}{R} \quad (2.25)$$

This is the **Stoney equation**. Values of stress in the film are determined through measurement of curvature  $R$  if other parameters are known.

Stress measured by Stoney method is an average stress since it is obtained by integrating the stress over the section or more precisely, over the thickness of the beam. If the thin film has an intrinsic stress or stress gradient, the Stoney calculated stress will be the average stress present at the middle of the beam, at the neutral axis, taking therefore into account, the effect of the gradient.

Compressive and tensile stresses in curved substrate vanish since stress is relaxed when bending. The stress is replaced by relaxed strain expressed in this case by the curvature of the substrate. Thanks to this curvature, the stress can be measured. Without it, it would be impossible to extract the residual stress because the film would stay constrained. The curvature measurement therefore gives the residual stress the thin film would have if it was not able to be relaxed.

Thanks to the simplifications ( $d_s \gg d_f$ ), only silicon Young's modulus and Poisson ratio must be known to extract the residual stress in any kind of thin films whatever the elastic properties of the film ( $E$ ,  $\nu$  and  $\alpha$  values). It makes this method very useful to measure residual stress in a thin film when we do not know their elastic properties. On the contrary, if strain in the thin film must be extracted, its Young's modulus and Poisson ratio must be known.

Without the previous simplification, Stoney could be more rigorously written as

$$\sigma_f = \frac{1}{6R(d_f + d_s)d_f} \left[ \frac{E_f d_f^3}{(1 - \nu_f)} + \frac{E_s d_s^3}{(1 - \nu_s)} \right] \quad (2.26)$$

requiring to know the complete elastic properties of the thin film we want to characterize. Calculations with experimental results in next part will demonstrate the validity of the previous simplification.

Validity of the Stoney equation implies that the substrate has transversal isotropic elastic properties with respect to the film. Using single crystal silicon substrates featuring moderately anisotropic properties ( $\langle 100 \rangle$  oriented wafers) satisfies this transverse isotropy argument [27]. Films must also be uniform in thickness and stress must be homogeneous and equi-biaxial over the entire substrate. The legitimacy of these assumptions depends on the deposition process. Films such as thermal oxide, LPCVD nitride or PECVD oxide under consideration have a great uniformity unlike sputtered films where homogeneity is precarious [27].

About the thin film approximation, we can read in [70] that Stoney equation is a good approximation for thicknesses ratio  $d_f/d_s$  smaller than 10%. This equation seems to fail for properly describing the variation of stress with thickness and cannot be used for thickness ratios larger than 10%. The cited paper proposes modifications to the original Stoney formula which does not require information on the layers modulus, to improve calculations for thickness ratios up to 40%. As we will see further, thickness ratio in our case will never exceed 0.3% and confirm our ability to use the original Stoney equation.

For a stack of  $n$  layered and continuous films of thickness  $d_{fi}$  on a substrate with a thickness  $d_s$  always greater than the total films thickness  $\sum_1^n d_{fi}$ , the total curvature is just the sum of the individual films contributions since moments are additive [59]. It therefore appears that each film independently interacts with the substrate without accounting for the presence of adjacent films or the stacking sequence of films in the composite structure [71]. The stress  $\sigma_{fi}$  in the film number  $i$  therefore yields

$$\sigma_{fi} = \frac{E_s d_s^2}{6(1 - \nu_s)} \cdot \frac{1}{d_{fi}} \cdot \frac{1}{R_i} \quad (2.27)$$

and the total stress  $\sigma_{total}$  in the  $n$  stacked films is

$$\sigma_{total} = \frac{E_s d_s^2}{6(1 - \nu_s)} \cdot \frac{1}{\sum_{i=1}^n d_{fi}} \cdot \sum_{i=1}^n \frac{1}{R_i} \quad (2.28)$$

The expression shows that the total substrate curvature consists of a linear superposition of the bending effects resulting from each of the individual films. In other words, the stress in each film is proportional to the partial curvature in the substrate due to this particular film [71].

Our experimental results will confirm that this **superposition principle of Stoney** can be very useful to predict the internal stress value in stacked thin films on substrate when we know only the internal stress in each individual film and without knowing the elastic properties of the composite films.

### 2.2.2 Experimental results

The starting substrates were three inch diameter P-type  $\langle 100 \rangle$  380  $\mu\text{m}$  thick bulk silicon wafers. Three different layers were grown on five silicon wafers as summarized in Table 2.2. The growth time of each identical layer was kept constant to allow accurate comparisons. The 400 nm thick thermal oxide was grown at 1000°C under a mixed  $\text{O}_2\text{-H}_2$  atmosphere while the 300 nm thick LPCVD nitride was deposited at 800°C with a stoichiometric  $\text{SiH}_2\text{Cl}_2/\text{NH}_3$  ratio of 0.33 to obtain a  $\text{Si}_3\text{N}_4$  nitride. The 300 nm thick PECVD oxide was deposited in a plasma of  $\text{SiH}_4+\text{N}_2+\text{N}_2\text{O}$  at 300°C and densified under  $\text{O}_2$  at 800°C during 30 min. Since thermal oxide and LPCVD nitride growth in the furnace on both sides of our wafers, we etched the back side nitride layer by plasma and the back oxide (the top side being protected by a photoresist) using an HF solution. The thickness of the deposited films was measured using an ellipsometer.

Table 2.2: Three different layers deposited on five wafers.

Wafer	Layer
#1	Thermal oxide
#2	LPCVD nitride
#3	PECVD oxide (densified and not densified)
#4	Thermal oxide + LPCVD nitride
#5	Thermal oxide + LPCVD nitride + densified PECVD oxide

The residual average stress in each film was extracted comparing the wafer curvature before and after deposition using a Dektak profilometer over a distance of 50 mm with a stylus force of 20 mg. The profilometer gives the maximal deflection  $h_{\text{max}}$  of the wafer surface over the length of the scale [72] as shown in Fig. 2.5.

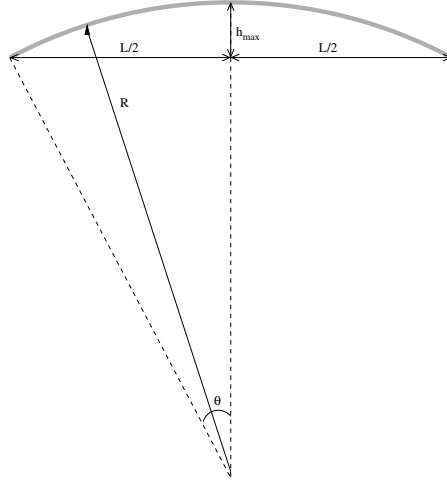


Figure 2.5: Evaluation of the radius curvature by profilometer scan.

From the schematic of Fig. 2.5, maximum deflection  $h_{\max}$  can be expressed as a function of  $R$

$$h_{\max} = R - R \cos \left( \frac{L/2}{R} \right) \quad (2.29)$$

For a small  $\theta$ ,  $R \gg L$ . With this approximation,  $\cos \left( \frac{L/2}{R} \right)$  can be simplified in the two first factors of its Taylor series. Eq. 2.29 becomes

$$h_{\max} = R - R \left[ 1 - \frac{1}{2} \frac{(L/2)^2}{R^2} \right] \quad (2.30)$$

and the curvature radius  $R$  can therefore be expressed as

$$R = \frac{\left( \frac{L}{2} \right)^2}{2h_{\max}} \quad (2.31)$$

where  $h_{\max}$  is the maximal deflection of the wafer surface and  $L$  the scanning length. Fig. 2.6 shows the curves obtained before and after the deposition and the difference between both curves.

As the film thickness  $d_f$  is much lower than the wafer thickness  $d_s$ , and the stress is isotropically distributed through the cross section of the film, one can use the Stoney



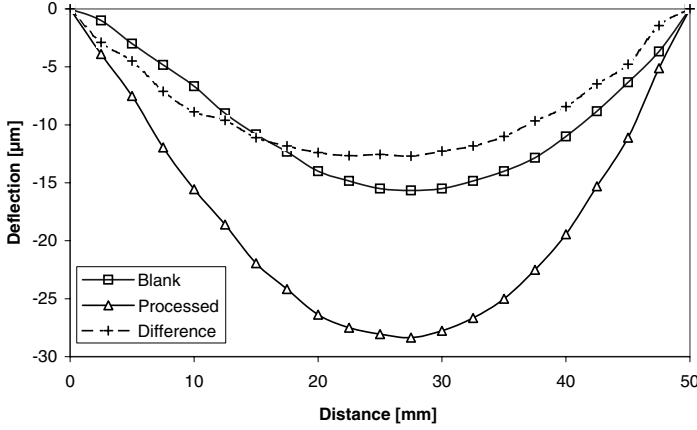


Figure 2.6: Curvature measurements for stress analysis in a stacking of thermal oxide, LPCVD nitride and densified PECVD oxide on a  $380 \mu\text{m}$  thick silicon wafer.

equation taking into account the initial  $R_{pre}$  and final curvature radius  $R_{post}$  measured before and after the deposition. The second term of the multiplication is now expressed as a radius variation rather than as the radius after deposition.

$$\sigma_f = \frac{E_s d_s^2}{6(1 - \nu_s) d_f} \cdot \left( \frac{1}{R_{post}} - \frac{1}{R_{pre}} \right) \quad (2.32)$$

A maximum deflection variation of around  $10 \mu\text{m}$  was measured on the wafers before the depositions. Following the classical convention, a minus sign was attributed to the radius of curvature for convex wafers (compressive stress) and a positive sign for concave wafers (tensile stress).

Table 2.3 summarizes our results. All values were measured for a starting  $380 \mu\text{m}$  thick silicon substrate using (100) silicon biaxial modulus of  $180.5 \text{ GPa}$  [60].

Table 2.3: Stress measurement in each layer.

Layer	Layer thickness [nm]	$R_{pre}$ [m]	$R_{post}$ [m]	Stress [MPa]
Thermal oxide	433	90.58	-45.29	<b>-331</b>
LPCVD nitride	288	54.16	13.24	<b>860</b>
PECVD oxide	283	23.15	57.87	<b>-397</b>
Densified PECVD oxide	283	23.15	31.25	<b>-172</b>

Stress values agree very well with published data (around -350 MPa for thermal oxide in [27], and between 700 and 1200 MPa for LPCVD nitride in [59]). As we will see in next part, these values will be confirmed by microstructures based measurements. The reproducibility of the method was also confirmed by the fabrication and measurements of independent batches. Thermal oxide and LPCVD nitride showed on other batches larger stresses (between -358 and -400 MPa for the first one and between 888 and 1080 MPa for the second one) always in the literature ranges. Finally delayed measurements do not show any shift (i.e. relaxation) over the time on the stress value at ambient temperature.

A calculation was made using the rigorous Stoney equation without simplification (Eq. 2.26) to check the validity of this simplification. Using values of elastic constants from Table 2.1, a stress of -312 MPa was calculated in thermal oxide, or a difference of 6%. But this error can also be due to incorrect elastic constant values used for the thin film.

It appears that the densification of the PECVD oxide drastically reduces its internal stress. The high value of the stress in PECVD oxide before its densification can be explained by the strong ion bombardments of the growing film by the plasma [59]. High RF power of bombardments results in films with higher density and lower etch rates very attractive in most microelectronics process, but with more compressive stresses. Works of [72] confirm and explain that annealing releases the nitrogen and hydrogen atoms trapped in the oxide and makes the oxide grains grow in size. It proceeds to a rearrangement of the atoms, increasing density of the oxide and decreasing its etch rate and its compressive stress.

The average stress in the previous stacked layers was also extracted. As shown in Table 2.2, sandwiches O-N (thermal oxide and LPCVD nitride) and O-N-O (thermal oxide, LPCVD nitride and densified PECVD oxide) were simultaneously realized following the same process with the previous layers. Measured results can be seen in Table 2.4.

Table 2.4: Stress measurement in stacked layers.

Layer	Layer thickness [nm]	$R_{pre}$ [m]	$R_{post}$ [m]	Stress [MPa]
<b>Sandwich O-N</b>	721	53.33	20.97	<b>174</b>
<b>Sandwich O-N-O</b>	1004	30.67	19.53	<b>80</b>

Our results indicate that the stacking appears as an interesting method to tailor the average stress and to build 1  $\mu\text{m}$  thick O-N-O membranes with a light tensile stress of

80 MPa. This value is a good compromise between surface planarity of the membrane to support all kind of sensors and robustness to be able to move up or down with a maximum of elasticity. It is confirmed by literature: we can read in [73] that from experiments, a thin-film residual stress must be lower than 100 MPa to have good mechanical properties.

Our stoichiometric LPCVD nitride shows a very large tensile stress and needs to be compensated using an oxide. Some other methods were proposed in the litterature to lower down the stress by increasing the silicon proportion in nitride, increasing the  $\text{SiH}_2\text{Cl}_2/\text{NH}_3$  ratio [74][73]. A ratio of four yields **silicon-rich nitride** ( $\text{Si}_1\text{N}_{0.85}$ ) with a residual stress of around 300 MPa which still constitutes a rather large stress. To decrease further more the residual stress, a three hours post oxidation step ambience is performed on this above mentioned LPCVD deposited silicon-rich-nitride to tune the film stress to a very low value of 10 MPa without introducing any stress gradient by the newly grown oxide. The paper concludes saying that this method could advantageously replace the sandwich structure (O-N-O) to perform very thin and large membranes (400 nm thick and as large as  $4 \times 4 \text{ cm}^2$ ).

**Oxynitride** films deposited by LPCVD from  $\text{SiH}_4/\text{N}_2\text{O}/\text{NH}_3$  gaseous mixture also seems to be an interesting alternative in producing very low stressed membranes as demonstrated in [75][76]. The gases ratio can be adjusted to perform a large range of residual stresses and very low stress can be obtained around the stoichiometric relationship  $\text{Si}_2\text{N}_2\text{O}$  (or  $\text{SiO}_{0.5}\text{N}_1$ ).

Nevertheless, when working on SOI (Silicon-on-Insulator) wafers, the 400 nm thick buried oxide is used as the first thermal oxide of our O-N-O stacking. Therefore, the previous methods cannot be interesting and the sandwich O-N-O still remains the best way to produce thin and low stressed membranes on SOI. In this process, nitride will be an added layer replacing the active silicon film and the last PECVD oxide will be the interconnection layer between polysilicon and metal. In the Unibond SOI wafers, the buried oxide is nothing else that a high quality thermal oxide bonded on another silicon wafer. Its residual stress was checked by wafer curvature method. The 100 nm thick silicon film was first etched in TMAH during 1 minute before the measurement of the final curvature radius  $R_{\text{post}}$ . Silicon oxide ( $4093 \text{ \AA}$ ) was then etched in HF and the initial curvature  $R_{\text{pre}}$  was measured. A value of **-363 MPa**, closed to stress measured in our thermal oxide, was finally calculated using Stoney equation taking into account the higher thickness of the SOI wafer ( $730 \mu\text{m}$ ) in comparison with the thickness of classical bulk wafers ( $380 \mu\text{m}$ ).

In case of stacked layers, we actually get a stress gradient due to the difference in stress values between the top and the bottom of the stacking. For instance, a stress gradient appears between the top nitride layer and the bottom oxide layer in O-N sandwich. But as explained above, Stoney always measures the average stress in this case. The gradient will be evaluated with dedicated cantilevers and will be widely reported in next section. It will also be explained how stress gradients can have an impact on the robustness of membranes realized from stacked layers.

We predicted the average stress in sandwiches by the superposition Stoney principle from the three isolated thin films. From Eq. 2.28 and Eq. 2.32 we have in case of two stacked films

$$\begin{aligned}\sigma_{ON} \cdot (d_O + d_N) &= \frac{E_s d_s^2}{6(1 - \nu_s)} \cdot \left[ \left( \frac{1}{R_{O_{post}}} - \frac{1}{R_{O_{pre}}} \right) + \left( \frac{1}{R_{N_{post}}} - \frac{1}{R_{N_{pre}}} \right) \right] \\ &= \sigma_O d_O + \sigma_N d_N\end{aligned}\quad (2.33)$$

where  $\sigma_{ON}$  is the average stress in the sandwich structure O-N of thickness  $(d_O + d_N)$ ,  $\sigma_O$ , the average stress in the oxide layer of thickness  $d_O$ , and  $\sigma_N$ , the average stress in the nitride layer of thickness  $d_N$ .

Using this previous equation, values of **144 MPa** and **55 MPa** are calculated respectively for O-N and O-N-O multilayers from the curvature values of the monolayers. The differences between the measured and calculated values are explained using the same Stoney superposition principle but starting from the sandwiches and decomposing them into isolated layers (by removing the partial stress from the total stress). Furthermore, this calculation will lead to some interesting conclusions about thermal behavior.

If the substrate curvature due to the stress in the densified PECVD oxide is subtracted from the substrate curvature due to the average stress in the sandwich O-N-O, a value of **179 MPa** is obtained for the stress in the sandwich O-N, very close to the measured value (**174 MPa**). It confirms that the deposition at 300°C of the PECVD oxide followed by a densification at 800°C does not affect the stress in the sandwich O-N underneath. It could be predicted since LPCVD nitride and thermal oxide were obtained respectively at 1000°C and 800°C.

Similarly, by removing the stress caused by the nitride layer from the stress of the sandwich O-N, one obtains the final stress in the thermal oxide. -281 MPa is calculated which is not so close to the -331 MPa directly measured in the oxide film. It could mean

that LPCVD nitride deposition affects the thermal oxide layer and removes a small part of its residual stress. To verify that, we put our oxidized wafer in the LPCVD oven to simulate nitride deposition at the same temperature during same time but without gas. The curvature measurements at the end of this test gave an average stress of -319 MPa. Temperature deposition of LPCVD nitride does therefore practically not affect the stress in thermal oxide layer as it could be expected since oxide was grown at a higher temperature than nitride. Temperature can therefore not be the reason for the decrease when nitride is actually deposited.  $\text{SiH}_2\text{Cl}_2$  and  $\text{NH}_3$  gases penetrating inside the oxide layer during the nitride deposition could maybe modify its internal structure and decrease its residual stress. More consistently, LPCVD nitride grown on silicon oxide seems to have a higher residual stress than LPCVD nitride grown on silicon due mainly to the difference in numbers of nucleation<sup>3</sup> sites between silicon surface and silicon oxide surface. As there are more nuclei growing on amorphous oxide than on cristalline silicon, resulting nitride grains are wider on silicon than on silicon oxide. And since stress is inversely proportional to the grains size [59], the stress in nitride layer deposited on silicon oxide is increased. So residual average stress in nitride deposited on oxide becomes therefore **914 MPa** instead of the lower value of 858 MPa. Nevertheless, the difference caused by the measurement of the nitride stress on substrate is only 6 % thanks to its already very high stress value.

This difference of stress in the LPCVD nitride layer deposited on oxide instead of silicon explains the difference between measured and calculated values of stress in case of sandwiches O-N and O-N-O. Taking into account the non negligible effect of the nucleation, the Stoney superposition principle has therefore demonstrated its ability to predict the average stress of a stack when the average stress of each constitutive layer is known.

The curvature method was finally used to measure the final average residual stress in a O-N-O membrane at the end of a complete gas sensor process. To perform that, the curvature of a wafer undergoing the process steps was measured before and after the process. The other layers besides the constitutive layers of the membrane were removed just after their deposition. The idea was to check if steps like polysilicon and aluminum deposition, annealing and etching could affect the average stress of a membrane. In this process, thermal oxide, LPCVD nitride and densified PECVD oxide were obtained in the same way as explained above but their thicknesses were slightly different: 430 nm for thermal oxide, 340 nm for LPCVD nitride and 390 nm for PECVD oxide. Previous values

---

<sup>3</sup>Nucleation can be defined as the initial stage in a phase transformation, evidenced by the formation of small particles (nuclei) of the new phase, which are capable of growing. Nucleation is always depending on the substrate surface [27].

of stress with the new thicknesses of these layers can be used to predict the final average stress using the superposition principle of Stoney. The thickness variation would have no impact on the previous stress values of LPCVD nitride and PECVD oxide since these layers are uniform through their thickness. It is a priori not the case for thermal oxide but its thickness is exactly the same than in our previous tests. Therefore, by Stoney superposition principle using stress values in Table 2.3 and new thicknesses, we foresaw an average stress around 100 MPa. 160 MPa were measured by wafer curvature on the test wafer at the end of the process. To explain this higher tensile stress, layers were removed one after the others, curvature measurements were performed between each etch and stress values were calculated using the superposition principle of Stoney. -174 MPa for densified PECVD oxide, 1027 MPa for LPCVD nitride and -332 MPa for thermal oxide were extracted by this way. These results reveal therefore that PECVD oxide and thermal oxide were not affected by the process given their values very close to the previous ones (see Table 2.3). Only the stress in LPCVD nitride, once again, was increased in comparison with the 915 MPa extracted above, giving an underestimation of the final tensile stress.

### 2.2.3 Discussions and summary

Substrate curvature method seems to yield a simple and fair estimation of the average stress in the three constitutive layers of our membrane as well as in their stacking. A low tensile average stress of 80 MPa was extracted in a O-N-O membrane and was found very close to the predicted value calculated using Stoney superposition principle on each isolated layers. By the decomposition of the sandwich to each isolated layers, we explained the physical behaviors at the origin of the differences between measured and calculated values. This method was finally validated by comparing the final measured average stress of the three stacked layers of our membrane at the end of our gas sensor process with the calculated expected value. It revealed that curvature measurement and its superposition principle can be very attractive to foresee the mechanical properties of multilayers.

Advantages and drawbacks of these methods can finally be summarized as following:

**Advantages of curvature measurement method:**

- Requires only fast and easy measurements,
- Does not need any photolithographic step,
- Gives the average stress of a thin film without a priori knowledge of its elastic properties (Young's modulus and Poisson ratio),

- Provides an average stress including the effect of the stress gradient,
- Can be used to predict the average stress of stacked layers from the knowledge of the average stress and the thickness of each of them.

**Drawbacks of curvature measurement method:**

- Provides the average stress value over the entire test wafer and does not take into account the local fluctuations on the wafer and the fluctuations from one wafer to another (since measurements are performed on a test wafer and not on the actual processed wafer),
- Requires elastic properties of the thin film under consideration to extract the average strain.
- Provides an average stress integrated over the whole thickness of a layer but does not quantify the stress gradient in it.

To complete this detailed study on the average residual stress measurements by wafer curvature measurement technique, it was needed to check if a complementary method compensating these drawbacks, could yield comparable results. The presentation and development of this complementary technique are the focus of the next section.

## 2.3 Strain measurements using micromachined structures

As explained above, substrate curvature measurements result in an average wafer level value of the stress rather than local values. Local stress does not necessarily mean the same as stress measured by substrate bending techniques, since stress is defined microscopically, while deformations are mostly induced macroscopically [27]. Residual stress can vary across a wafer but also from a test wafer to a processed wafer and from lot to lot. It is therefore essential to quickly accurately access local residual stress values during and after wafer processing. Local measurements have also the advantages that measurements are made on the same dimensional scale as the film of interest and that the local stress field can be mapped [77].

The local film strain can be measured using in situ micromachined structures made directly out of the film of interest itself. When a thin film structure under stress is released by removing the underlying silicon, the residual stress in this structure is relaxed and is converted into a measurable increase or decrease of the structure dimensions. This deformation is the relaxed strain proportional to the stress included in the thin film before its relaxation. The proportionality factor in this case is the uniaxial Young's modulus since each microstructure presented in this section are characterized by a length much longer than its width [78][79][65]. Moreover, our microstructures are subject to uniaxial compression or traction and the beam sides are free for most of the length. Young's modulus is therefore required to extract the final average stress from the measured strain if necessary. But on the contrary to the curvature measurement method, the microstructures presented in this section yield measurements of the strain without the knowledge of the elastic constants of the silicon substrate and the measured thin film.

Nevertheless, both methods will be compared since the elastic constants of the silicon and the three dielectric layers in consideration are known with good accuracy. But the strain of a layer having unknown elastic constants would be advantageously extracted from microstructures and the stress from curvature method to finally calculate the Young modulus and Poisson ratio of this layer for instance. Both methods remain therefore complementary. To perform accurate comparisons, in the following, each local film stress measurements was performed on layers deposited during the same process than for previous curvature measurements (on same wafers than wafers in Table 2.2).

The change in length when the microstructure is relaxed is however very small, making direct measurement difficult. It is therefore necessary to convert this change into buckling of a part of the structure or into a larger displacement. The buckling of a clamped-clamped beam appears above a critical compressive stress. The stress is estimated from the maximum length possible without buckling and requires therefore an array of devices with incrementally increasing lengths. In another way, to increase a displacement we can transform the extension or contraction of a supported beam due to the strain in a rotation of a second beam. The deflection of the tip of this beam will be a few times larger than the extension or contraction of the primary beams and is an indication of the strain value in the structural layer. These structures will be presented in next paragraphs.

While contact profilometer was used to perform substrate curvature measurements in our lab<sup>4</sup>, only nocontact optical methods are necessary to measure the strain in released

---

<sup>4</sup>Note that substrate curvature can be measured by no contact methods such as laser scanning.



structures. Scanning electron microscopy (SEM) and optical microscopy were used for in-plane measurements. But for thin films, normal mode of buckling is out-of-plane. Optical microscopy can be used to perform that but it requires focal plane adjustments which are not really accurate for small deflections. Microscopic interferometry [80] is a more sensitive technique for detecting small buckling. A home made interferometric setup based on a low coherence light emitting diode (LED) source was used [81][82] and was seen powerful. The principle of this technique is detailed in Annex B with illustrations acquired during our measurements.

Finally, it could be interesting to note that in our case, the micromachining is at the middle way between surface and bulk micromachining since silicon bulk is partially etched to release the thin films structures. All structures were especially designed to take into account the TMAH silicon etching property, i.e. the undercutting of masking material at convex corners (see previous Chapter).

### 2.3.1 Clamped-clamped beam and ring-and-beam structures analysis

#### Theory

A doubly supported beam (Fig. 2.7) under compressive stress will buckle when it is released. An array of this kind of microstructures with various lengths can be therefore used to estimate a range of **compressive strains** by determining which of them have buckled at a given stress level [11]. The critical strain  $\varepsilon_{cr}$  can be estimated in this case using the Euler equation for a critical buckling beam of length  $L_{cr}$

$$\varepsilon_{cr} = \frac{\pi^2 h^2}{3L_{cr}^2} \quad (2.34)$$

where  $h$  is the beam thickness, and  $L_{cr}$ , the critical beam length (i.e. the shorter beam at which buckling occurs). So, for a given layer thickness, a higher stress leads to a shorter critical buckling beam and reverse. However, if the layer thickness  $h$  decreases, the critical buckling length  $L_{cr}$  decreases in the same way.

Furthermore, as the amplitude of the buckling is sensitive to residual stress in the film, this allows each buckled beam to be used for residual strain measurement  $\varepsilon_C$  in the

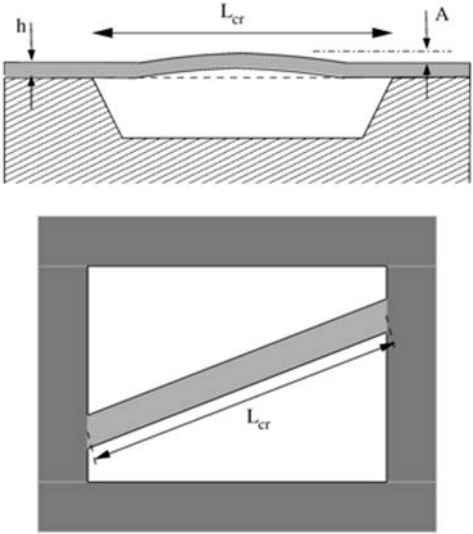


Figure 2.7: Cross view and top view of a clamped-clamped beam released on silicon. The beam was drawn obliquely across the silicon cavity to be released by silicon anisotropic etching (see later).

post-buckling regime [54]. Residual strain for each buckled beam can be determined from

$$\varepsilon_C = \frac{\pi^2}{12L^2} (3A^2 + 4h^2) \quad (2.35)$$

as demonstrated in details in [54] and [78] where  $A$  is the amplitude of the buckling deflection,  $L$  is the beam length and  $h$  is the beam thickness. The shape of the buckling beam is sinusoidal as exposed by [54]. Both  $A$  and  $h$  can be accurately measured by interferometry and ellipsometry respectively, and  $L$  is well-known from the layout dimensions. Eq. 2.35 gives excellent results for the residual strain measurement using beam of lengths somewhat larger than the ideal critical Euler buckling length  $L_{cr}$  [54]. We will see further that it is very interesting in our case where films thicknesses are very thin showing very short buckling lengths for a given critical strain and therefore difficult to be detected by optical interferometry.

To accurately extract the effect of the strain gradient on clamped-clamped beam deflection, the full deflection curve was compared in [54] with a two-dimensional finite difference model. It was found from these simulations that for the post-buckled beams, use of Eq. 2.35 rather than the more complete model results in less than a 3% difference in the residual strain results. This indicates that the effect of the gradient on the residual strain measurements is small on post-buckled beams. The further going into the post-buckled regime, the less the gradient affects the buckled geometry and therefore the measured residual strain. On the other hand, the model shows that gradient affects the evaluation of the transition and prebuckled beams [54]. It is one more motivation to use the post-buckling measurement in case of thin film thermal oxide for instance since it contains internal strain gradient.

A microstructure under residual tensile stress is more difficult to be relaxed when it is released to express its **tensile strain**. So, the idea was therefore to design a structure transforming the tensile stress into a compressive stress which could lead to a measurable deformation or strain. The structure performing that is the ring as shown on Fig. 2.8. In this structure, a circular ring anchored at two diametrically opposite positions converts tensile residual stress into compressive stress in a crossbeam that is orthogonal to the ring anchors [54]. A tensile stress in the layer deforms the ring into an ellipsoid, and the stress in the central beam becomes compressive. Ranges (rather than precise measurements) of residual strain levels are determined by observing the transition from unbuckled to buckled crossbeams as for clamped clamped beams.

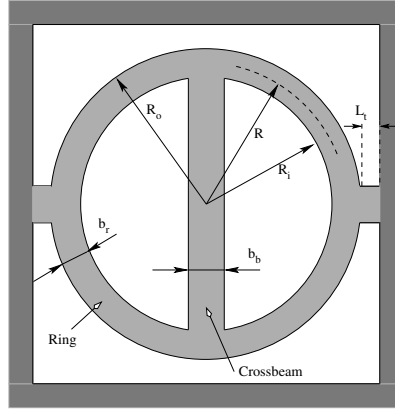


Figure 2.8: Top view of a ring-and-beam structure ready to be released on top of the silicon cavity.

The residual strain for the structure is

$$\varepsilon_R = \frac{\varepsilon_{cr}}{g(R_{cr})} \quad (2.36)$$

where  $\varepsilon_{cr}$  is the critical strain needed to buckle the crossbeam and  $g(R_{cr})$  is the conversion efficiency of tensile strain in the first buckled ring into compressive strain in the crossbeam.

The critical strain  $\varepsilon_{cr}$  can be approximated to be the same as the critical buckling strain in the clamped-clamped beam from Eq. 2.34 where the length of the beam  $L_{cr}$  was expressed in terms of ring radius ( $L_{cr} = 2R_i$ ). This is not completely true since the crossbeam or buckling beam in the ring structure is not clamped at the ends. The ends will even move due to the deformation of the ring when it converts the tensile strain in the layer into a compressive strain on the beam [11]. [83] calculates the exact value of  $\varepsilon_{cr}$  taking into account the out-of-plane torsion of the ring. With the previous approximation, Eq. 2.36 yields:

$$\varepsilon_R = \frac{\pi^2 h^2}{12 \cdot R_i^2 \cdot g(R_{cr})} \quad (2.37)$$

The conversion efficiency  $g(R_{cr})$ , is found from the following equations [83] [54]:

$$g(R_{cr}) = \frac{-(2b_r f_2)}{(2b_r f_1 + b_b f_1^2 - b_b f_2^2)} \quad (2.38)$$

$$f_1 = \left(\frac{\pi}{4} - \frac{2}{\pi}\right) \left(\frac{R_{cr}}{e}\right) - \frac{2e}{\pi R_{cr}} + \frac{4}{\pi} - \frac{\pi}{4} + \frac{\pi k_f (1 + \nu)}{2} \quad (2.39)$$

$$f_2 = \left(\frac{1}{2} - \frac{2}{\pi}\right) \left(\frac{R_{cr}}{e}\right) - \frac{2e}{\pi R_{cr}} - \frac{1}{2} + \frac{4}{\pi} - k_f (1 + \nu) \quad (2.40)$$

Definitions of the geometrical parameters  $b_r$  and  $b_b$  can be found in Fig. 2.8. The constant  $k_f$  is a form factor for transverse shear ( $k_f = 1.2$  for rectangular cross sections [83]),  $\nu$  is the Poisson Ratio,  $R_{cr}$  is the effective ring radius, and  $e$  is the eccentricity,

$$e = R_{cr} - \frac{b_r}{\ln\left(\frac{R_o}{R_i}\right)} \quad (2.41)$$

with

$$R_{cr} = \frac{(R_o + R_i)}{2} \quad (2.42)$$

$$R_i = R_{cr} - \frac{b_r}{2} \quad (2.43)$$

$$R_o = R_{cr} + \frac{b_r}{2} \quad (2.44)$$

With a scaled array of ring-and-beam test structures, the approximate value of the residual tensile film stress can therefore be determined by observing for which length crossbeams have buckled.

It seems important to note that the strain gradients affect the bending of microrings, meaning that the entire shape and not only the crossbeam flexures must be measured in order to correctly interpret the deformation of the structure [54]. In fact, a tensile state would only be indicated by significantly different out-of-plane flexures for the crossbeam compared to the ring. Without the complementary information from the cantilevers to detect any strain gradient, we could incorrectly conclude that if the crossbeams were buckled, the residual strain in the film was tensile. But as we will see further, in our case, tensile LPCVD nitride does not show any gradient which could be at the origin of erroneous measurements.

### Experimental setups and results

As it has been mentioned in the previous theoretical part, in case of our two buckling structures, an array of structures is needed to be able to measure strains within a defined range.

From literature and from our previous results using wafer curvature method, we know that the compressive stress in thermal or PECVD oxide can vary around -350 MPa. From its well known Young's modulus of 70 GPa and using the Hooks law (Eq. 2.6), the proportional strain range was evaluated between 0.1 and 1 %. Equivalent critical lengths were calculated using Eq. 2.34 in the range of 7 to 23  $\mu\text{m}$  (using  $h = 433 \text{ nm}$  from Table 2.3). However, longer beams were designed to make measurements in post-buckling state until 50  $\mu\text{m}$ . All beam lengths in the array have been carried out in several beam widths of 3, 5 and 8  $\mu\text{m}$ . Theoretically, the beam width has no effect on critical strain (it does not appear in Eq. 2.34) but in practice, it is not really the case.

In the same way, tensile stress values in stoichiometric LPCVD nitride are generally around 1000 MPa, either a strain value around 0.37 % (with a Young's modulus of 270 GPa). An array was designed around this value of strain from 0.1 to 1 % for three ring-and-beam width ratio (i.e.  $b_r/b_b$  ratio): 3/5, 4/2 and 3/2. From Eq. 2.37 and following (with  $\nu = 0.27$  and  $h = 288 \text{ nm}$ ), the ring radius  $R$  was therefore calculated in the range of 7 to 40  $\mu\text{m}$ . The tie length  $L_t$  was fixed equal to 0.5 or 1  $\mu\text{m}$  (depending on the ring size) as close to zero as possible since equations were designed without ties. Finally, for drawing the masks, rings were approximated in polygons by dividing the circle into 22 straight lines.

Tables 2.5 and 2.6 summarize both designed arrays.

Table 2.5: Clamped-clamped beam array.

<b>width</b> [ $\mu\text{m}$ ]	<b>first length <math>L</math></b> [ $\mu\text{m}$ ]	<b>last length <math>L</math></b> [ $\mu\text{m}$ ]	<b>step</b> [ $\mu\text{m}$ ]	<b>#</b>
3	7	50	0.70	62
5	7	50	0.70	62
8	7	50	0.70	62

As silicon is used as sacrificial layer, it was needed to take into account the properties of anisotropic silicon micromachining by TMAH for their design. Thanks to its property

Table 2.6: Ring-and-beam array.

width ratio $b_r/b_b$	first radius $R$ [ $\mu\text{m}$ ]	last radius $R$ [ $\mu\text{m}$ ]	step [ $\mu\text{m}$ ]	#
5/3	7.5	11.5	0.1	57
	11.5	15	0.5	
	15	20	1	
	20	40	5	
4/2	7	11.5	0.1	62
	11.5	15	0.5	
	15	20	1	
	20	40	5	
3/2	6.5	10	0.1	50
	10	12	0.5	
	12	20	1	
	20	40	10	

of undercutting of masking material at convex corners (see previous chapter), clamped-clamped beams were therefore drawn obliquely at  $45^\circ$  across the cavity to be released without damaging the anchors (as shown of Fig. 2.7). As it will be demonstrated further, this special geometry could slightly underestimate the measured strain but Eq. 2.34 and 2.35 always remain valid. In this case, length was measured between both anchors, at the middle of the beam as shown in Fig. 2.7 to give an average length.

On the other hand, rings do not need any special configuration because their intrinsic geometry involves convex angles allowing the complete structure to be released in TMAH without damaging the anchors.

The fabrication process to release our structures was in this case easier than a classical process to release polysilicon structures on sacrificial layer. Only one mask and one photolithography step are needed. After growing the thin film on the silicon substrate, structures were defined by photolithography and patterned using the appropriate etchant (plasma for nitride and PECVD oxide, HF for thermal oxide). Wafers were then put in HF during 10 seconds to remove native oxide on silicon before TMAH etching. Silicon etching was performed in a TMAH 20% solution at  $90^\circ\text{C}$  just long enough to release the complete structures; i.e. during one hour, providing a cavity depth of around  $60\text{ }\mu\text{m}$ . Wafers were finally rinsed in DI water and dried in methanol in place of classical rinser dryer to avoid structures damage.

Buckling detection was first performed using focal plane adjustments of optical microscopy to give an approximate value of average stress in our thin films. But this tech-

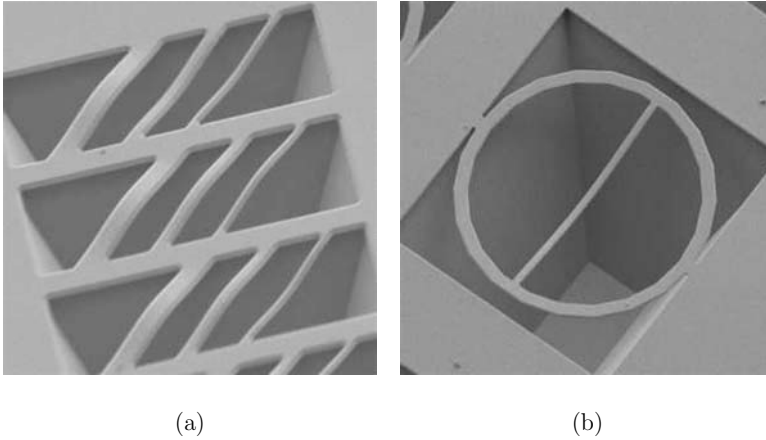


Figure 2.9: (a) SEM view of the last nine clamped-clamped beams of the array (as defined in Tables 2.5 and 2.6) in thermal oxide and (b) last LPCVD nitride ring-and-beam (radius  $R = 40 \mu m$ ,  $b_r = 4 \mu m$  and  $b_b = 2 \mu m$ ).

nique was demonstrated to be not so relevant due to the really small dimensions of our beams. In order to increase their dimensions and therefore their visibility, the solution could be to increase their thickness. Nevertheless, thicker layers are difficult to obtain and would lead to a different internal structure (due to their intrinsic stress for instance) and therefore, not to the same average stress. Interferometry was therefore preferred as shown in Fig. 2.10 and 2.11.

In the case of **thermal oxide**, the detection of the critical buckling beam was impossible. The very low thickness indeed resulted in a too small critical beam for a high residual stress as shown in Eq. 2.34. However, we observed a decrease of the buckling at the end of the array, i.e. for stresses around -400 MPa. Moreover, oxide has an intrinsic gradient which could alter the detection of the critical buckling beam as explained above. Therefore, measurements were performed on post-buckled beams by interferometry from the 12th to the 62nd beams for each of the three widths to analyze the effects of the length and the width. Obtained profiles can be seen on Fig. 2.12.

Strain was calculated from the amplitude of the deflection using Eq. 2.35 and stress was extracted using the Young's modulus of thermal oxide (70 GPa). Variations of calculated stress versus the beam lengths and widths are depicted at the top of the graphic in Fig. 2.13 and yield an average stress value between -280 and -330 MPa.



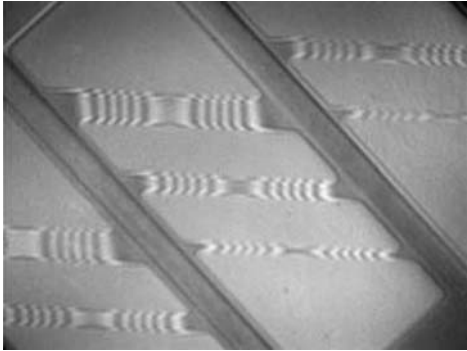


Figure 2.10: Interferogram of thermal oxide 50  $\mu\text{m}$  long clamped-clamped beams.

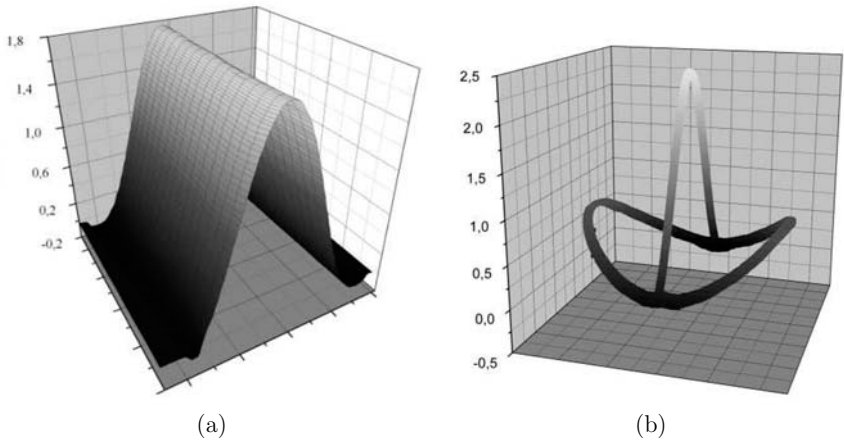


Figure 2.11: Tridimensional view of the deflection (in  $\mu\text{m}$ ) extracted by interferometry: (a) clamped-clamped beam and (b) ring-and-beam structure.

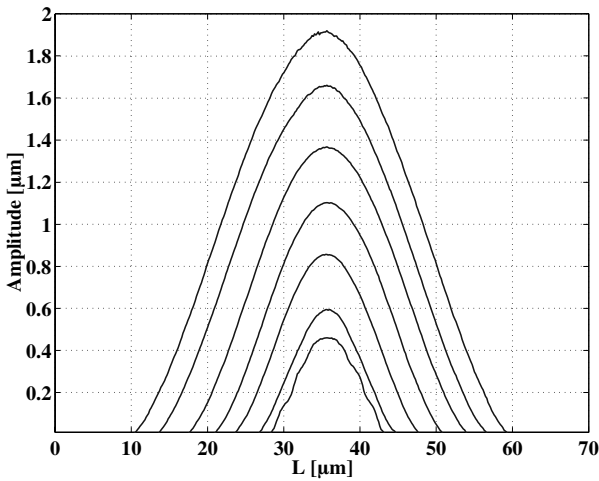


Figure 2.12: Thermal oxide clamped-clamped beams deflection for one width of 5  $\mu\text{m}$  and 7 different lengths: 50.20, 44.55, 37.48, 31.11, 25.46, 19.80, 17.68  $\mu\text{m}$ .

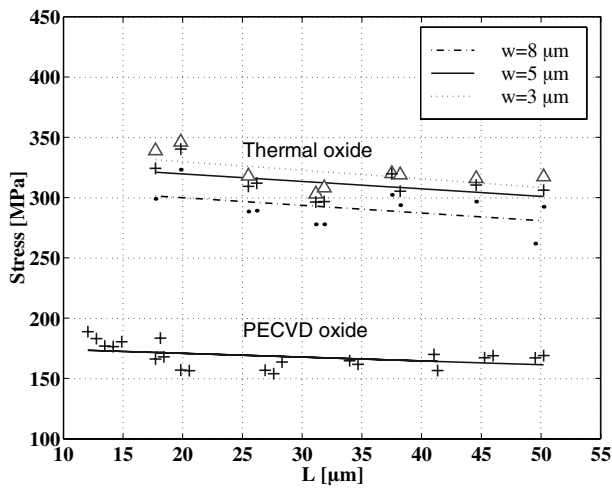


Figure 2.13: Measured stress on clamped-clamped beam array vs. length of the beam for 3 different widths in case of thermal oxide and for a beam width of 5  $\mu\text{m}$  in case of PECVD oxide.

Stress appears slowly decreasing when the length increases. This could be due to the fact that the stress gradient has a large influence on the buckling of shorter beams and less effect as the beam gets longer. Regarding the difference of stress versus the width of the beam, a wider beam shows a lower stress than a narrow beam. We will make the same analysis on cantilevers at the end of this chapter, i.e. wider beams have a greater stiffness and would therefore be less relaxed than narrower beams. The geometry of the beam clamped obliquely also provides a little more rigidity to the beam near their anchors. It was confirmed by ABAQUS mechanical simulations: a higher stress concentration was observed at the anchors. This effect decreases of course with the beam width and in borderline case, it vanishes when the beam width is close to zero. So, the medium width ( $5\text{ }\mu\text{m}$ ) seems a good trade-off between medium stiffness, great measurement facility and low error induced by the geometry. Finally, measurements of  $5\text{ }\mu\text{m}$  wide beams on other sites showed an average range of stress values (for beams of  $35\text{ }\mu\text{m}$  long) between **-300** and **-330 MPa**.

Compressive strain in **densified PECVD oxide** was also characterized using clamped-clamped beams array. As the strain measurement is depending on the thickness of the layer, we took into account the fact that PECVD oxide was attacked significantly in TMAH on the contrary of thermal oxide and LPCVD nitride (see previous chapter). A thickness of  $275\text{ nm}$  was measured after one hour of etching giving also an expected critical buckling beam impossible to be detected. Measurements were therefore performed by interferometry on  $5\text{ }\mu\text{m}$  wide post-buckled beams and gave an average stress between **-160** and **-190 MPa** as shown at the bottom in Fig. 2.13.

The detection of the critical buckling crossbeam in the array of rings was finally performed by interferometry to measure the tensile stress in **LPCVD nitride**. First buckling crossbeam was initially impossible to detect since each crossbeam and each ring of the array appeared buckled. But measurements of the deflection height on three points of the ring-and-beam structure (on the anchor, at one extremity of the crossbeam and at the middle of the crossbeam) revealed an interesting behavior: the deflection of the crossbeam had its sign changing once accross the array. Therefore, the critical buckling was extracted by detecting the sign change in the crossbeam deflection. The absolute deflection of the crossbeam was extracted removing from its value the heights of the anchor and of one extremity of the crossbeam. The graphic in Fig. 2.14 shows the evolution of the absolute deflection of the crossbeam versus the critical stress calculated for each ring from its ring radius (with a Young's modulus of  $270\text{ GPa}$ ). The second curve shows this proportionality between the calculated critical stress and each ring radius. It clearly

depicts that the crossbeam deflection changes sign in this case around 990 MPa.

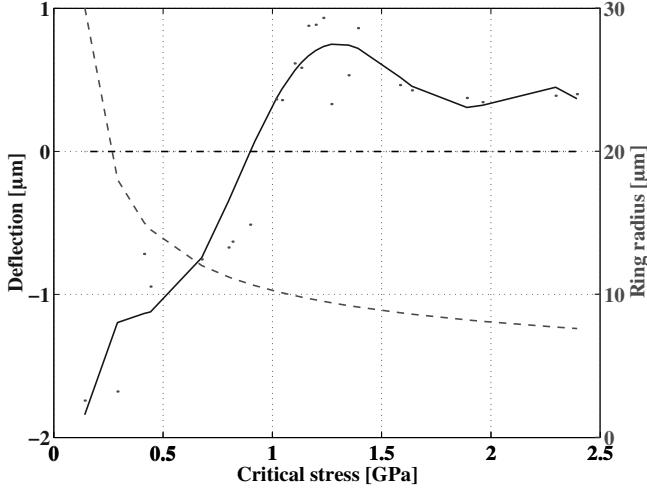


Figure 2.14: Absolute deflection of the crossbeam versus critical stress calculated for each ring from its ring radius (second curve).

Detection therefore became very easy to perform. This way, measurements were carried out over the wafer and showed stresses in the range from **840** to **1015** MPa with a higher repeatability of values on the left of this range. The best reproducibility was reached for the 4/2 width ratio showing the higher difference between the beam and the ring width. The measurement also showed a large difference in buckling amplitude between the ring and the crossbeam demonstrating that no gradient was present [54]. This will be demonstrated further using cantilevers.

### 2.3.2 Microgauges analysis

Both clamped-clamped beams and ring-and-beam structures need to be implemented in entire arrays of structures and they could not be so easily integrated with active microstructures due to space constraints. In contrast to previous structures, only one microgauge is sufficient to determine any **tensile or compressive strain** under optical microscope independently on the deposited thin film thickness [55][27].

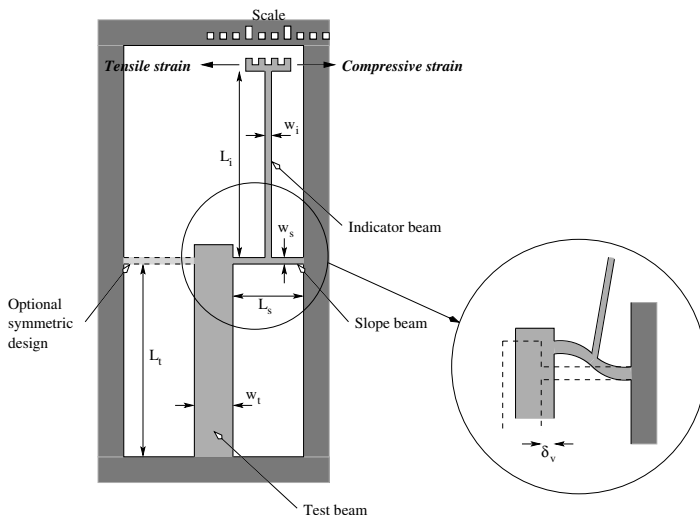


Figure 2.15: Microgauge designed to be released on silicon and zoom of the slope beam when a high compressive stress occurs.

As shown in Fig. 2.15, the microgauge consists of three beams, a test beam, a slope beam, and an indicator beam. All of them are suspended above the substrate to move freely but are anchored at two points, one at the end of the test beam and another at one end of the slope beam. Residual strain existing in the thin film causes the test beam to either expand (under compressive residual strain) or contract (under tensile residual strain). This movement is transferred to the slope beam causing its deflection into an “s” shape (see Fig. 2.15) since the other end of the slope beam is a fixed anchor. The indicator beam, which is placed at one end at the center of the slope beam, amplifies this tiny rotation in a large displacement of its other end where is placed a scale (or a vernier) to simplify the reading of the deflection under microscope. A compressive stress moves the indicator beam to the right due to the elongation of the test beam and a tensile stress leads to a deflection to the left. Fig. 2.15 depicts that a second slope beam can be put on the opposite side of the test beam with another anchor. This symmetrical design shows the same strain readout than the one-sided design [55] but the added anchor gives more rigidity to the structures fabricated in very thin films. A disadvantage of this modified structure is that it buckles easier since residual stress in the slope beam cannot be relaxed.

The residual strain in the test beam measured by the deflection of the indicator is

demonstrated in details in [55] and can be represented as

$$\varepsilon_g = \frac{2L_{sb}\delta_v}{3L_{ib}L_{tb}C} \quad (2.45)$$

where  $L_{sb}$ ,  $L_{ib}$  and  $L_{tb}$  are respectively the lengths of the slope beam, the indicator beam and the test beam, respectively.  $\delta_v$  is the measured deflection read from the gauge scale.  $C$  is a correction factor due to the presence of the indicator beam and is derived as

$$C = \frac{1 - d^2}{1 - d^3} \quad \text{with } d = \frac{w_{ib}}{L_{sb}} \quad (2.46)$$

where  $w_{ib}$  is the width of the indicator beam.

The accuracy of the microgauge is greatly improved because its output is independent on the film thickness but also on the cross-section of the microstructure which could have a trapezoidal shape after a wet etching. Finally, the strain measurement with this kind of microstructure is not affected by the out-of-plane strain gradient. However, in presence of high intrinsic strain gradient, the movable part of the indicator bends upwards, and it is difficult to focus the microscope to both scales simultaneously.

Similarly to clamped-clamped beams and rings, the gauges were released by etching silicon underneath with TMAH. As the structure involves a lot of convex corners, a rectangular cavity was straightforwardly etched under the structure, three sides providing the anchors and the fourth side providing the reference scale as shown by the SEM picture in Fig. 2.16. The etching time was more critical to control in this case to avoid undercutting of the anchors during beams release. One hour was shown optimal and yielded sufficiently deep cavities (around 60  $\mu\text{m}$ ) to avoid any stiction problem.

In our case, no vernier was integrated on the tip of the indicator beam as it is usually performed in gauges [55] but only a scale corresponding to another reference scale on silicon to be able to measure the displacement by SEM. It was easier to design and more suitable in our case of very thin dielectric films. Due to the very low thicknesses of our layers, in spite of an accurate design, the vernier would be deformed and laterally etched, leading to incorrect reading of the strain.

Several dimensions were tested but only one gauge was completely released after one hour of etching and gave good results. Its dimensions are summarized in Table 2.7. They result of a trade-off between high precision in the measured strain range, great stiffness of the structure after its etching and complete release of the three beams in a short time

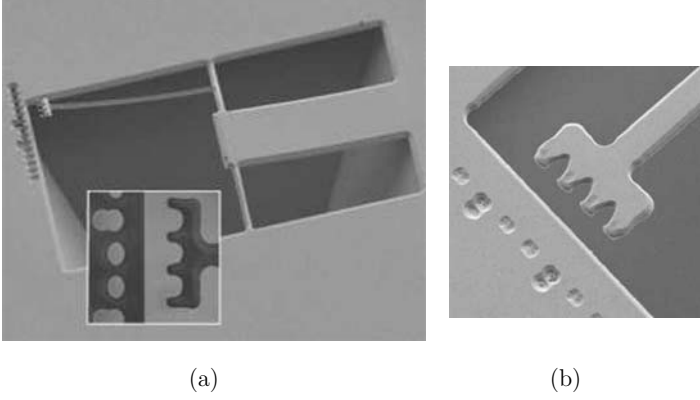


Figure 2.16: (a) SEM view of a gauge in thermal oxide and (b) zoom of the tip of a LPCVD nitride gauge (for dimensions, see Table 2.7).

without damaging the anchors. Moreover, the notches at the top of the indicator beam scale and on the reference scale were chosen with a width of  $1\text{ }\mu\text{m}$  and a separation of  $1.5\text{ }\mu\text{m}$  considering the limitations of the optical photolithography.

Table 2.7: Design values of the microgauge.

$\mathbf{L_{tb}}$	$\mathbf{L_{ib}}$	$\mathbf{L_{sb}}$	$\mathbf{w_{tb}}$	$\mathbf{w_{ib}}$	$\mathbf{w_{sb}}$
$[\mu\text{m}]$	$[\mu\text{m}]$	$[\mu\text{m}]$	$[\mu\text{m}]$	$[\mu\text{m}]$	$[\mu\text{m}]$
53	50	20	20	2	2

Displacements of the indicator beam were measured using SEM imaging. An optical microscope in its maximum magnification (100X objective) would be sufficient but even without gradient (in case of LPCVD nitride), the thin indicator beam tended to buckle a little out of plane giving large out of focus problems. Measurements were achieved on several sites to determine a range of stress instead of a constant value. Thermal oxide exhibited deflections from  $1.20$  to  $1.30\text{ }\mu\text{m}$  rightwards (measured by SEM) which reported in Eq. 2.45 and 2.46 lead to values of stress from **-460** to **-490 MPa** (with Young's modulus of  $70\text{ GPa}$ ). Indicator beam in LPCVD nitride was deflected to the left from  $0.58$  to  $0.70\text{ }\mu\text{m}$  showing a tensile stress from **795** to **950 MPa** (with Young's modulus of  $270\text{ GPa}$ ). Gauges in PECVD oxide did not give reproducible results due to their damaging during TMAH etching. When the thin beam was released during etching, the beam continued to be damaged from the top as from the bottom and the side walls of

the beam. So, the thickness and the width of the indicator beam decreased slowly during etching and finally tended to be a useless wire distorted in all directions.

An alternative interesting microstructure derived from the microgauge is proposed by [56]. It consists of a pair of two cantilever test beams with different lengths connected by a short indicator tip beam. The difference of contraction or elongation between the two test beams under strain causes the deflection of the indicator beam. The errors in displacement measurement due to the stress gradient or the nonvertical side walls (which can appear after some wet isotropic etching) effects are demonstrated negligible. As shown in [56], the advantage of this structure in comparison with the classical microgauge is that it does not need the slope beam to amplify the movement and therefore gives measurements without the errors it introduces. A symmetrical design is also presented to measure a double displacement. This structure was tried with success in our lab to make strain evaluation in 2  $\mu\text{m}$  thick polysilicon layers using a sacrificial oxide layer. Nevertheless, its geometry is less compatible with the anisotropic wet etching to release the underlying silicon substrate without damaging the anchors and this method was therefore not chosen for the present purpose.

### 2.3.3 Cantilever beams analysis

#### Monolayer cantilever beams

Previous microstructures were shown useful to measure uniform compressive or tensile strain. We studied the limitations of these structures when some non uniformities or stress gradients occur through the depth. It is therefore very important to measure if a stress gradient exists in the structural layer to verify the validity of our measurements with the previous microstructures. Moreover, it is interesting to see if changing some parameters in the process steps of the layer deposition could result in a smaller intrinsic stress gradient. The cantilever will allow us to perform this measurement as it will be demonstrated below.

Fig. 2.17 shows a cantilever beam clamped at one side, built in a thin film (thickness  $h$ ) with an intrinsic stress gradient, deposited on silicon substrate. Before the cantilever release, there is both an average stress (compression) and a stress gradient in the thin film. The average stress is a thermal mismatch stress between the thin film and the substrate and the stress gradient is an intrinsic stress in the thin film. If we suppose the film is released but constrained to stay flat, the average stress would go to zero since



the film would be free to expand or contract. The uniform stress would in this case be replaced by a uniform relaxed strain. But the film would stay in tensile stress on top and compressive stress at the bottom and therefore in stress gradient. Without such constraints, the freestanding film will curve towards the side that is in tensile (positive) stress until the stress is relaxed. The stress gradient is then vanished and replaced by a relaxed strain gradient. The curling of the cantilever can therefore be used to measure this relaxed strain gradient.

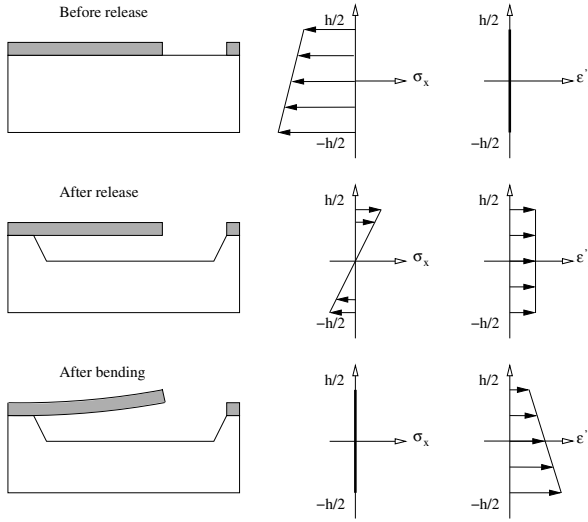


Figure 2.17: Curvature caused by stress gradient in freestanding thin film of thickness  $h$ . Diagram of approximated stress and relaxed strain  $\epsilon'$  (as defined above) through the thickness.

We can consider the radius of curvature as a function of strain gradient or more precisely as a function of stress gradient since the cantilever will curve from the constraint state (under stress gradient) to the completed relaxed state as shown in Fig. 2.17. This is a particularly simple case in which the treatment of a cantilever beam exactly follows that of a plate (as demonstrated at p. 56), assuming that the biaxial modulus needs to be replaced by the uniaxial modulus. From Eq. 2.20 calculating the maximum stress on top and at the bottom of the film, we can therefore extract the stress gradient  $\Delta\sigma$  (or the strain gradient  $\Delta\epsilon$ ) as the difference between the stress at the top ( $+\sigma_m$ ) and bottom

( $-\sigma_m$ ) assuming that the stress variation between these two limits is linear:

$$\Delta\sigma = E \frac{d}{R} \quad \text{or} \quad \Delta\varepsilon = \frac{d}{R} \quad (2.47)$$

where  $d$  is the thickness of the film under consideration and  $R$  the radius of curvature.

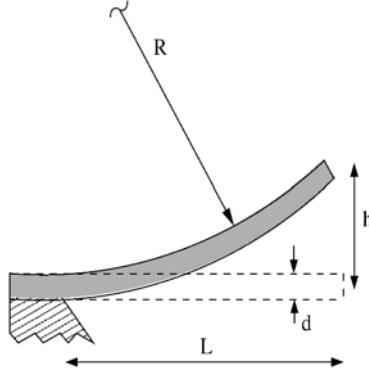


Figure 2.18: Relaxed cantilever beam under strain gradient.

As demonstrated in p. 62, radius of curvature  $R$  can be extracted from Eq. 2.31 where  $L/2$  in case of the curvature of a total wafer is replaced by  $L$  for a deflected cantilever and  $h_{\max}$  replaced by  $h$  (see Fig. 2.18),

$$R = \frac{L^2}{2h} \quad (2.48)$$

From Eq. 2.47 and 2.48 we can express the stress gradient  $\Delta\sigma$  per unit of thickness  $d$  as

$$\frac{\Delta\sigma}{d} = E \frac{2h}{L^2} \quad (2.49)$$

where  $\frac{\Delta\sigma}{d}$  is expressed in Pa/ $\mu\text{m}$  or MPa/ $\mu\text{m}$  [84]. A cantilever beam exhibiting a concave shape, i.e. a bending away from the substrate, is associated with a positive stress gradient. A negative stress gradient is associated with cantilever beams bending towards the substrate, i.e. a convex beam [57].

In comparison with the substrate curvature method (Stoney equation) where the stress is integrated over the whole thickness of the film, the cantilever equation only gives the

difference of strain between the top and the bottom of the thin film. In both cases, stress is transformed to a curvature when the film is relaxed. Thanks to some simplifications, Stoney equation gives the stress without the knowledge of the biaxial modulus but it remains useful for extracting the average strain. On the contrary, in case of cantilevers, the strain gradient is first calculated and the Young's modulus of the film remains useful for extracting the stress gradient.

The beam curves in a circle of radius  $R$ , a long beam will describe a longer part than a shorter one, and a high stress gradient will curve the cantilever with a lower radius than a lower stress gradient. One length of cantilever will cover a wide range of stress gradients but if its deflection becomes higher than its radius  $R$ , it will not be measurable anymore. So, an array of cantilevers is needed to allow the measurement of a large range of stress gradient. A high stress gradient needs for short beam to be measured. On the other hand, long beams will be useful to measure lower stress gradient.

Cantilevers were processed similarly to the previous microstructures taking into account the undercutting properties of silicon by TMAH at convex corners. All beams in the array have been carried out in four widths: 2, 5, 10 and 15  $\mu\text{m}$ . Theoretically, the beam width has no effect on the stress gradient but in practice, it is not completely the case as shown for clamped-clamped beams. Wider beams were showing a slightly lower deflection than narrow beams due to their higher stiffness probably. It is not so critical in our case where only relative measurements are interesting for the comparison of the strain gradient between two locations or between two processes. Therefore, measurements will always be performed on same widths.

Deflections  $h$  were measured using optical microscope comparing the focusing on the two tips of the cantilever. Deflections of 12  $\mu\text{m}$  were measured for 100  $\mu\text{m}$  length and 10  $\mu\text{m}$  wide cantilevers made in thermal oxide, giving a radius of curvature  $R$  equal to 416  $\mu\text{m}$ . A strain gradient of 0.24  $\%/ \mu\text{m}$ , i.e. a stress gradient of 170  $\text{MPa}/\mu\text{m}$  for thermal oxide was calculated therefrom. For a thickness lower than 1  $\mu\text{m}$  (0.4  $\mu\text{m}$ ), it is more clear to express this value as 17  $\text{MPa}/0.1 \mu\text{m}$ , i.e. a difference of stress between the top and the bottom of the layer of 68  $\text{MPa}$ .

In comparison with the average stress measured in thermal oxide (-331  $\text{MPa}$ ) over the total thickness, the 68  $\text{MPa}$  represent only the variation of stress between the top fiber and the bottom fiber of the layer. The previous measurement methods gave only an average stress in thermal oxide, the stress on the neutral fiber at the middle of the layer as shown in Fig. 2.17 (before release). When a cantilever is released, the average stress is

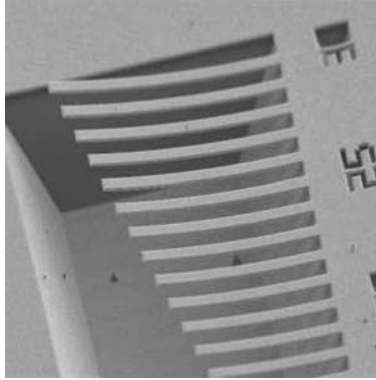


Figure 2.19: SEM view of an array of  $10\text{ }\mu\text{m}$  width cantilevers builded in thermal oxide on etched silicon cavity. Longest showed beam is  $150\text{ }\mu\text{m}$  long.

removed because the beam is free to elongate or shrink without introducing any visible deformation. A cantilever therefore only measures the stress gradient which is exhibited when the cantilever curves to its relaxed position. So, the total stress in thermal oxide can be expressed as  $-331 \pm 34\text{ MPa}$ .

Measurements were also performed with interferometry giving the profile shown in Fig. 2.20. Measurements were possible only for short beams ( $50$  and  $70\text{ }\mu\text{m}$ ) featuring low deflections due to the lack of field depth in case of too high out-of-plane displacements. To increase the depth of field, a lower magnification must be chosen leading to a lack of lateral precision and contrast. But in extrapolating the two results we have obtained by quadratic interpolation, we were able to extract the radius of curvature of the beams. By this way, our last result of  $12\text{ }\mu\text{m}$  of deflection for  $100\text{ }\mu\text{m}$  long beam measured previously by optical microscopy was confirmed.

In other way, we observed as shown in Fig. 2.21 a large discontinuity at the beginning of the beam near the anchors. This is physically inconsistent but can be explained as followed: the light is reflected on the silicon side of the cavity instead of being reflected on the transparent beam. This phenomenon occurs only close to the anchors where the distance between the beam and the silicon layer is shorter. To calculate the profile of the beam and the maximum deflection, we therefore must take it into account summing the minimum and the maximum deflections of the beam. We observed the same behavior for clamped-clamped beams and calculations were performed in the same way.

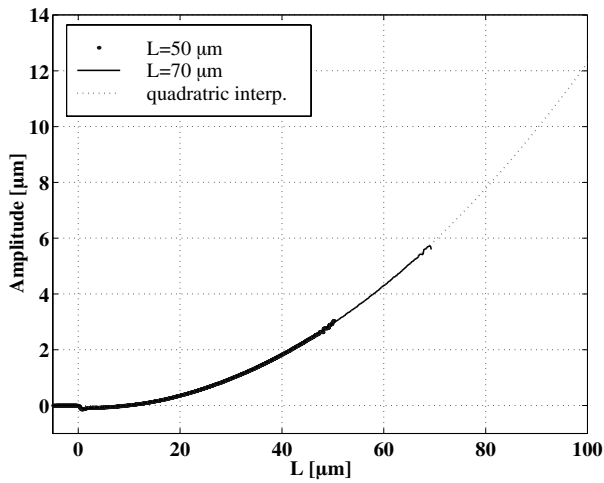


Figure 2.20: Thermal oxide  $5 \mu\text{m}$  width cantilever profile for two lengths and quadratic interpolation showing the curvature of the beam.

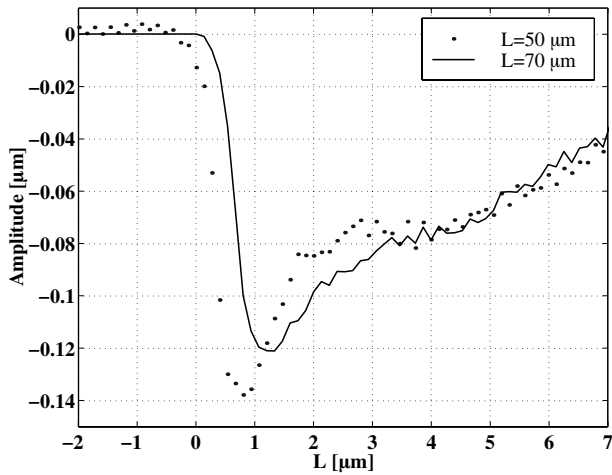


Figure 2.21: Detailed view of the discontinuities appearing between the anchor and the beginning of the beam.

Our calculations of the stress gradient from cantilevers structures are in fact a mathematically calculated average value. This value results in a similar deflection curve to that of the actual stress profile. The stress profile throughout the sample can be very complicated and depends a lot on the growth. Thus, a change in stress in a very small section of the layer can have an important effect on the deflection and, correspondingly, on the determined measured stress gradient [57]. We indeed supposed a linear stress profile between the top and the bottom of the oxide film since our calculations only give the difference of stress from the top to the bottom of the film. For the physical explanation of the stress behavior inside the layer, it could be therefore attractive to determine a complete stress profile throughout the thickness to show that profile is not so simple. As stress gradients become particularly acute as the film becomes thinner [77], an idea consists in measuring the stress gradient in a film at different thicknesses by progressive thinning [84][57]. The stress profile through the thickness can be calculated by this way from the values of the stress gradient. Afterwards, the average stress of the measured profile can be confirmed as the total stress in the thin layer. But due to the limited vertical resolution of this technique, this method is increasingly inaccurate for thinner layers [57].

We generally assume that average stress has no effect on the bending of a cantilever. Fang and Wickert [77] demonstrate the opposite. The portion of the beam clamped to the substrate (the anchored end) undergoes some in-plane deformation (expansion or contraction) under an average stress. The deformation of this portion of the film bonded to the substrate leads to a slight rotation of the released cantilever at the anchored tip as modeled in [77]. This phenomenon is exploited to find the total residual stress. So, under a combination of average stress and stress gradient as in thin oxide layers, a released cantilever will deflect out-of-plane, with its far field curvature being exclusively generated by the stress gradient (as measured above) and with an initial slope determined by both the average stress and the stress gradient. Characterization of the measured deflections by interferometric profilometry in this manner allows to estimate the total residual stress using the model of [77]. Only one single cantilever instead of a complete array is needed in this case to measure simultaneously average stress and stress gradient. But as observed in [57], the measurement of the slope of the beam at the suspension is very complicated and time-consuming and on the other hand, the effects of the rotation introduce very small error in the stress gradient value. Moreover in our case, the discontinuities occurring under interferometric measurements at the anchored tip of the beam do not allow to confirm this slope. For these reasons we did not consider it in our analysis.

This previous method can be extrapolated to improve the accuracy of the bilayer

method [68]. The bilayer method consists in depositing the thin film layer of interest on a cantilever beam used as a base material so as to form a bilayer sandwich-like structure. The stress level in the film layer is then deduced by measuring the deflection of the bilayer cantilever taking into account the initial curvature of the base cantilever measured prior to the film layer deposition. This technique is especially useful to characterize very thin films that are not stiff enough to be used as cantilever beams. Nevertheless, as the thin film must be deposited after the release of the base layer, this technique is only usable for metallic sputtered films.

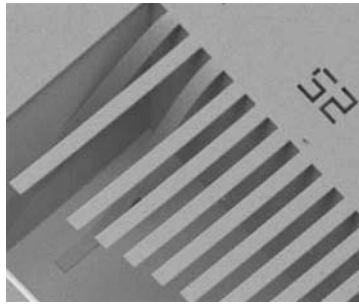


Figure 2.22: Stiction appearing between nitride cantilever and silicon on the bottom of the cavity after water rinsing and drying in methanol.

Finally, it appears interesting to us to introduce the main problem appearing in the fabrication of this kind of suspended cantilever beams which is known as the **stiction**, i.e. the permanent adhesion of the beam to the substrate if their surfaces come into contact. The phenomenon is usually divided in two stages: first, a mechanical collapse mainly caused by the attractive capillary forces, and second, a permanent adhesion to the silicon substrate caused by the hydrogen bonding [85]. Hydrophilic silicon has a large number of surface -OH groups so that hydrogen attraction occurs between silicon and suspended cantilever when fluid as water, nitrogen or oxygen is trapped in the gap, causing their sticking [11][86]. The use of methanol, which has a lower surface tension than water, can be applied after the final water rinse to displace the water [86]. It reduces the stiction but does not avoid it completely as depicted in Fig. 2.22 showing two nitride cantilevers sticking on the bottom of the silicon cavity after methanol rinsing. The best way to suppress this effect is the use of critical point drying to dry the samples after their rinsing. This method takes advantage of the fact that, under the correct conditions of temperature and pressure (the “supercritical region”), the liquid and vapor phases cease existing as

distinct states. When this occurs, the interface between them is eliminated and, after transitioning directly to the gas phase, the gas can be gently vented without disturbing the structures [11]. In this process, the wafers immersed in methanol are brought into a pressure vessel at room temperature. Liquid CO<sub>2</sub> is then used to replace methanol during a rinse cycle. The temperature of the liquid CO<sub>2</sub> is then raised above its critical point and the pressure vessel is finally vented and the CO<sub>2</sub> gas escapes. A liquid to solid interface is never formed during the process, and hence surface tension is completely suppressed [86].

### Multilayer cantilever beams

Stress gradient can be intrinsic as shown above but can also appear when two or more layers (with uniform or non-uniform stress) are stacked together due to the difference between the average residual stress of each film in the multi-layer. In this case, stress gradient is mainly caused by a gradient in the thermal expansion coefficient of the stacking layers. So the magnitude and sign of the resulting stress gradient can be different for each combination of films [65]. In this case, the stress gradient is more difficult to extract since we need to know the Young's modulus of the stacking to calculate the stress gradient from the strain gradient. Nevertheless, the strain gradient can be calculated using the following equation derived from Eq. 2.49:

$$\frac{\Delta\varepsilon}{d} = \frac{2h}{L^2} \quad (2.50)$$

where  $d$  is in this case the total thickness of our multi-layer.

An average Young's modulus of the stacking is difficult to extract. The stacking is not an alloy and it would be wrong to calculate an average Young's modulus (of the combination) as the linear interpolation between each constitutive layer (as calculated in [84] for SiGe layers for instance). In [65], the Young's modulus of stacked films is measured on composite cantilevers by nano-indentation. It is presented as a technique to determine the Young's modulus of each thin film constituting the composite stack, without accessing the individual layers during processing. To perform that, the summation formula  $E_{av}I_{av} = \sum_{j=1}^n E_j I_j$  is used where  $E_{av}$  and  $I_{av}$  are respectively the Young's modulus and the moment of inertia of the stacking, and  $E_j$  and  $I_j$ , the individual Young's modulus and the moment of inertia of the  $j$ th film. A different formula to calculate the average Young's modulus is presented in [79] as  $E_{av}A_{tot} = \sum_{j=1}^n E_j A_j$  where  $A_j$  and  $A_{tot}$  are respectively the area of the  $j$ th material in the cross section and the total cross sectional area.



The calculation of an average Young's modulus is a solution more or less accurate to extract the stress gradient from the strain gradient. A more rigorous solution would be to measure the complete stress profile through the thickness of the combination by progressive thinning as exposed above. It is nevertheless very complicated to implement and not really necessary in our case. The direction of the cantilever deflection, its measurement and the calculation of the strain gradient is enough for us.

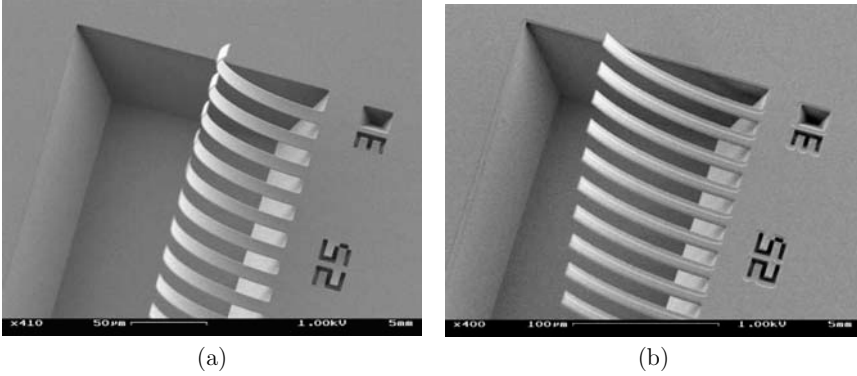


Figure 2.23: SEM view of an array of  $10\ \mu\text{m}$  width cantilevers built in ON (a) and ONO (b) stacking.

Strain gradient measurements were performed on O-N and O-N-O sandwich structures. Both combinations showed positive stress gradient, or a deflection away from the substrate as shown in Fig. 2.23. The deflections were measured by focal plane adjustments on optical microscope but could not be confirmed by interferometry as explained above. As observed when measuring gradient in oxide layer, wider beams showed always a lower deflection than narrow beams probably due to their higher stiffness. Measurements were performed on same width ( $10\ \mu\text{m}$ ) for more relevant comparisons. A radius of curvature going from  $94$  to  $104\ \mu\text{m}$  was measured for O-N cantilever beams having a deflection smaller than their radius of curvature (before the 25th as shown on Fig. 2.23(b)), i.e. a strain gradient from  $0.96$  to  $1.06\ \%/ \mu\text{m}$ . In the same way, we measured a radius of curvature from  $128$  to  $130\ \mu\text{m}$  for O-N-O sandwiches leading to a strain gradient from  $0.77$  to  $0.78\ \%/ \mu\text{m}$ .

As shown in Fig. 2.23(b), PECVD oxide on top of the cantilever was overetched sideways during the etching of the thermal oxide due to the lower density and the higher etch rate of PECVD oxide versus thermal oxide. This problem can not be avoided but is

not critical since the outcoming geometry does not affect the measurement of the strain gradient. It is clearly visible also that the combination O-N-O has a lower strain gradient than the same combination without PECVD oxide (O-N). It confirms that densified PECVD oxide added on the top of the structure leads to a compensation of the average stress and the stress gradient in the structure.

Table 2.8 summarizes the results of our strain and stress gradients measurements. We were able to extract the stress gradient from the thermal oxide only thanks to the knowledge of its Young's modulus. On the other hand, only strain gradient could be measured for the other layers and layers combinations. LPCVD nitride and PECVD oxide did not show any significant strain gradient.

Table 2.8: Approximated values of strain and stress in mono and multi-layers for a given cantilever width.

Layer	strain gradient [%/ $\mu\text{m}$ ]	stress gradient [MPa/ $\mu\text{m}$ ]	curvature
<b>Thermal oxide</b>	0.24	170	+
<b>LPCVD nitride</b>	negligible	negligible	/
<b>PECVD oxide</b>	negligible	negligible	/
<b>Sandwich O-N</b>	1.01	/	+
<b>Sandwich O-N-O</b>	0.78	/	+

### Discussion on multilayer membranes

The strain gradient measured in O-N-O combination is the same strain gradient as the one expected in our membranes. In static equilibrium, it will not affect the robustness of the membrane, it is just interesting to know that the top is in average more tensile than the bottom as demonstrated by the cantilever. If the membrane is subjected to a load from the top or from the bottom, things will be different. The membrane will tend to buckle up or down under the force or the pressure in spite of the fact that the membrane is tensed by an average internal tensile stress (of +80 MPa). If the membrane curls up (Fig. 2.24), the top layer will be more elongated than the bottom layer (due to a higher radius of curvature) and therefore subject to a more compressive stress than the bottom layer. Forced buckling in this case will compensate the positive stress gradient present in the stacking. On the contrary, if the membrane is curling down, the opposite will occur, resulting in an additive compressive stress at the bottom. In this case, cracks could appear in oxyde layer if deflection is too high but could be stopped by the nitride layer at the

middle of the stacking thanks to its high tensile stress. In the case of our application, the membrane will curl up due to the displacement caused by the heating microheater (see chapter 1 of part III) and could therefore be expected to be more robust in our case than a unilayer membrane.

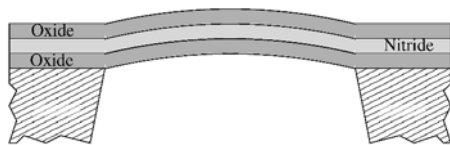


Figure 2.24: Membrane under deflection.

To finish, it can be interesting to note here that a pressure applied on a micromachined membrane can be used to evaluate directly its average stress. A differential pressure applied across the diaphragm causes its bowing outward. The vertical displacement at its center is then measured using an optical interferometer and is related to the stress [1]. This method could be attractive in our case to directly extract the average stress in our performed membrane (at the end of a gas sensor process for instance) but it is complicated to perform and needs to know the Young's modulus and the Poisson ratio of the stacking to extract the final average stress. Moreover, calculations derived from equation shown in [1] are complicated and need to find geometry constants. The previous studied methods will therefore remain the best combination even to extract the stress in a membrane.

### 2.3.4 Summary and outlook

Clamped-clamped beams and ring-and-beam arrays gave accurate results requiring only interferometry to perform out-of-plane deflection measurements. On the other hand, microgauge measurements need SEM imagery to measure the displacement of the tip of the indicator beam reported to the scale. Both methods were confirmed easy to perform. The accuracy of the first method is limited only by the precision of the layer thickness measurement. In the second method, the measurement is independent on the layer thickness but it can be less accurate when the gauge and its scales are overetched, as shown in Fig. 2.16(a).

Using clamped-clamped beams in post-buckling state tends to slightly underestimate the actual compressive stress value probably due to the oblique geometry of the beams

as explained above. However measured values on thermal oxide are reproducible with a narrow dispersion as expected for a high quality thermal oxide. Ring-and-beam structures showed a wide variation of stress value across the wafer due to the lower quality of the deposited LPCVD nitride film and the limitation of the method accuracy. The overestimations observed for oxide gauges in comparison with results obtained by previous methods are probably due to patterning problems occurring during HF etching and to the high stress gradient present in thermal oxide. Again results are consistent and relatively constant on the whole wafer as shown previously with beams. Results in LPCVD nitride agree reasonably well with the range measured using rings-and-beam structures thanks to the higher resolution of the nitride plasma etching and its lack of stress gradient. Finally, cantilevers showed a significant intrinsic stress gradient present in our thermal oxide monolayer and how the stacking of multilayers with different average stress can affect the final stress gradient of a beam or a membrane.

Realizations of dielectric clamped-clamped beams or cantilevers using sacrificial etching of silicon can be found in literature [79][65][27][78]. However, most of the time these structures are based on isotropic etching of silicon. In this work, complete arrays of dielectric clamped-clamped beams, ring-and-beams, microgauges and cantilevers were released for the first time using anisotropic TMAH etching instead of isotropic etchants. TMAH etching requires a wise design to take into account its undercutting properties but gives at the end a better control of the anchored tips without a critical control of the etching time. Microstructures are therefore easier to process while giving more reproducible results.

Our microstructures array was also used to characterize stress in pure evaporated **aluminum**. It is out of the scope of this chapter but is interesting to note for the following reason. Aluminum microstructures can not be built on sacrificial oxide layer due to the very bad selectivity of HF versus aluminum. It is the same for most isotropic and anisotropic silicon etchants making difficult the use of silicon as sacrificial layer. In our case, thanks to our improved TMAH solution giving a high selectivity versus aluminum, we can use the previous microstructures to characterize this material. Microgauges measurements were performed on 900 nm thick evaporated aluminum layer. Measurements yielded values varying around zero from **-80 to +70 MPa**, therefore either compressive or tensile. These values were confirmed by wafer curvature measurements yielding values between -30 and +60 MPa. Regarding results of the literature, we find in [27] that aluminum has a low melting point and a corresponding high diffusion rate even at room temperature and is usually fairly stress free. Our stress values varying around zero seem therefore consistent. However, in comparison with measured values for dielectric

layers, we observed a wide dispersion across the wafer and a non reproducibility from one process to another. An explanation of these dispersions would be the high solubility of the silicon into the pure aluminum film affecting its properties and its homogeneity. It could be better therefore to deposit a very thin oxide layer on silicon before the aluminum evaporation which could be removed at the end without damaging aluminum to perform the measurements. Another solution would be to deposit an aluminum doped with 2 % of silicon by sputtering as used in standard IC processes. But sputtered metals can be expected to be more stressed as confirmed in [59].

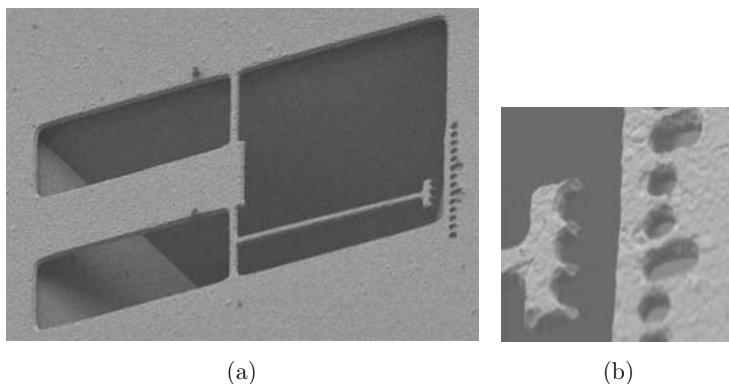


Figure 2.25: Stress measurements in aluminum layer on silicon as sacrificial layer (a) microgauge in aluminum and (b) detail of the tip of the indicator beam.

It would be possible to characterize nitride using oxide as sacrificial layer thanks to the great selectivity of the oxide etchant (HF) versus nitride. The experiment was not performed for a thin tensile nitride layer but for a compressive thicker **polysilicon** layer for which we have no other choice. We focused especially on microgauges [55] and clamped-clamped beams as depicted in Fig. 2.26. A  $2.5\ \mu\text{m}$  thick polysilicon layer deposited at  $625^\circ\text{C}$  under 90 sccm of  $\text{SiH}_4$  was investigated. Deflection to the right of  $4.72\ \mu\text{m}$  was measured on the microgauge and buckling was detected on the clamped-clamped beam area between lengths of 100 and  $150\ \mu\text{m}$  (Fig. 2.26). Both methods gave finally the same strain value around 0.13 % or a compressive stress value of **-210 MPa** using a Young's modulus of 160 GPa. This value is difficult to compare with literature due to the wide variety of polysilicon layers but is in good agreement with measurements performed by wafer curvature method over several processes (around between -180 and -220 MPa).

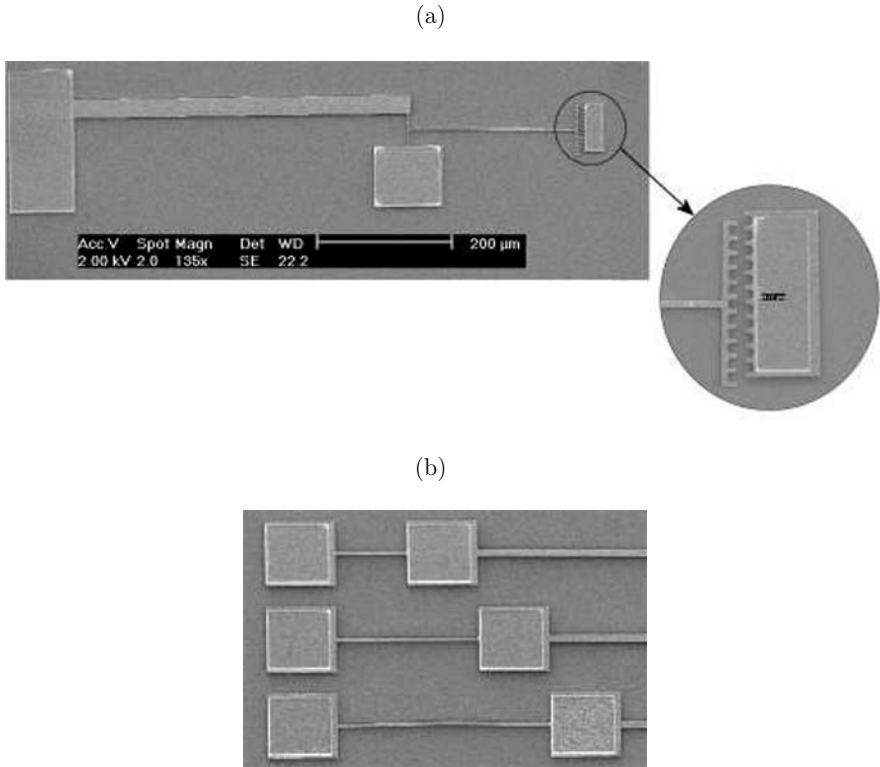


Figure 2.26: Stress measurements in polysilicon layer using oxide as sacrificial layer (a) microgauge with  $L_{tb} = 500 \mu\text{m}$ ,  $w_{tb} = 30 \mu\text{m}$ ,  $L_{sb} = 50 \mu\text{m}$ ,  $w_{sb} = 3 \mu\text{m}$  and  $L_{ib} = 250 \mu\text{m}$ ,  $w_{ib} = 4 \mu\text{m}$ ; (b) part of the clamped-clamped beam array (width  $3 \mu\text{m}$ ) around the critical beam, lengths are respectively from the first to the last  $50$ ,  $100$  and  $150 \mu\text{m}$ . The buckling is clearly occurring between the second and the third beam.

In comparison with microstructures fabricated on silicon, in this case, a sacrificial layer must be deposited and patterned using an additional mask. A  $2\text{ }\mu\text{m}$  thick PECVD oxide layer was deposited as sacrificial layer, and patterned with HF to define the anchors of the future microstructures. This step is critical and depends strongly on the density of the used oxide. A weakly densified oxide will be easier to release at the end than a dense oxide but will be more damaged sideways during the etching of the  $2\text{ }\mu\text{m}$  thick anchors. A densified PECVD oxide having an etch rate around  $100\text{ nm/min}$  seems a good compromise for this purpose. After this etching, polysilicon was deposited and patterned by plasma. The release of the microgauges and clamped-clamped beams was performed in wet HF, rinsed in water and finally dried in methanol. Stiction was a critical problem in this case due to thin gap between the suspended microstructure and the substrate. Methanol is one solution but vapor HF releasing [87] or critical point drying would be more effective.

Microstructures using oxide as sacrificial layer are the unique solution to measure stress in polysilicon since polysilicon layer would be completely etched during a potential silicon release. But if we have the choice as for nitride for instance, the use of silicon as sacrificial layer remains more powerful. Silicon release is more economical in time and in materials, it avoids stiction problems, and the critical patterning of anchors is by-passed. Another drawback of the use of oxide as sacrificial layer is due to the thin gap between the suspended beams and the substrate. Stress in very thin films is more difficult to measure since they buckle more often out of the plane and are for this reason more attracted to stick on the substrate when buckling downward. It is therefore needed to characterize films thicker than the film of interest. The measurement will remain valid in the absence of stress gradient but if a gradient occurs, the measured average stress will be not so consistent. It is the case in polysilicon layer as demonstrated in the literature [27].

To conclude, the new techniques presented here to extract the stress using microstructures present a lot of advantages as compared to most realizations proposed in literature:

- Anisotropic etching avoids geometric problems at the anchors and tedious control of the etching time,
- Silicon used as sacrificial layer is more economical in terms of time and cost since it uses only one photolithographic step and only one mask, it also allows the ability to measure stress in layers as silicon oxide,
- The formation of deep cavity under the microstructures avoids stiction problems,

- The high selectivity of our TMAH based solution allows to extract the stress in aluminum layers,
- The characterization of the film in its actual thickness gives more accuracy, especially when stress gradient is present.

## 2.4 Final conclusions

An in-depth study of the stress and stress gradient in thin dielectric films was performed and explained along this chapter. After a theoretical recall of the mechanics involved in thin films, two well known methods were demonstrated and developed by experiments from a new approach. Both methods allow for stress measurements on dielectrics layers using the same thin dimensions as in target applications and for this reason, a small area was needed to integrate microstructures arrays. Stress and strain gradient in multilayers were also measured to be able to finally extract the average stress and strain gradient in a stacked dielectric membrane to predict its robustness. Silicon was chosen as sacrificial layer allowing the extraction of the stress in oxides and microstructures release was performed anisotropically instead of isotropically for a lot of detailed advantages.

Two methods were shown complementary: microstructures allow microscopic and local stress measurements and can be integrated in situ in any processed wafer, while curvature method gives average macroscopic results and needs additional test wafers to be added to the processed ones. Table 2.9 summarizes our results, demonstrating that both methods gave relatively similar results thanks to the homogeneity and the high quality of the films of interest. The overestimation of the stress measured using oxide gauge and the under estimation of the clamped-clamped oxide beams were explained by the high stress gradient present in the film.

Table 2.9: Summary of our stress measurements results.

Layer	Average stress [MPa]			Strain gradient [%/ $\mu\text{m}$ ]
	Stoney	Bridge/Ring	Gauge	
Thermal oxide	-331	-300...-330	-460...-490	0.24
LPCVD nitride	860	840...1015	795...950	0
Dens. PECVD oxide	-172	-160...-190	x	0
Sandwich O-N	174	x	x	1.01
Sandwich O-N-O	80	x	x	0.78



Both methods can therefore be compared and used according to the test purpose. Curvature measurements will calculate a value of the average stress without needing knowledge of the elastic constants of the film under interest, while microstructures will extract the average strain in the film. The first method also allows to measure exclusively the average stress in multilayers, while the second allows to extract the actual strain gradient value in these multilayers.

In our case, average stresses were calculated from the measured strain values using well established elastic constant values. But these constant values can vary from one piece of equipment to an other as well as between two processes. Difference in stress values extracted from wafer curvature measurements and microstructures could therefore be explained from a non accurate knowledge of materials properties. However, the strain of a layer having unknown elastic constants could be advantageously extracted from microstructures and the stress, from curvature method, so that finally, the Young modulus and Poisson ratio of this layer can be calculated. The complementary of the two methods is therefore fully demonstrated.

We also measured an average stress of -363 MPa in the buried oxide of a Unibond SOI wafer. We demonstrated by this measurement that this layer can advantageously replace the first thermal oxide layer of our membrane for gas sensors applications. Finally, one wafer was used to follow all steps of a gas sensor process to finally measure by wafer curvature technique, an approximation of the expected stress in the future membrane of our gas sensor. For more accuracy in next processes, we could put arrays of microstructures on the wafer to extract the final average stress and the strain gradient in each layer constituting our multilayered membrane.

Micromachined Thin-Film Sensors for SOI-CMOS  
Co-Integration

Laconte, J.; Flandre, D.; Raskin, J.-P.

2006, XIV, 292 p., Hardcover

ISBN: 978-0-387-28842-0